Robust Ellipse Fitting Using Hierarchical Gaussian Mixture Models

Mingyang Zhao, Xiaohong Jia, Lubin Fan, Yuan Liang, and Dong-Ming Yan

***Abstract*— Fitting ellipses from unrecognized data is a fundamental problem in computer vision and pattern recognition. Classic least-squares based methods are sensitive to outliers. To address this problem, in this paper, we present a novel and effective method called *hierarchical Gaussian mixture models* (HGMM) for ellipse fitting in noisy, outliers-contained, and occluded settings on the basis of *Gaussian mixture models* (GMM). This method is crafted into two layers to significantly improve its fitting accuracy and robustness for data containing outliers/noise and has been proven to effectively narrow down the iterative interval of the kernel bandwidth, thereby speeding up ellipse fitting. Extensive experiments are conducted on synthetic data including substantial outliers (up to 60%) and strong noise (up to 200%) as well as on real images including complex benchmark images with heavy occlusion and images from versatile applications. We compare our results with those of representative state-of-the-art methods and demonstrate that our proposed method has several salient advantages, such as its high robustness against outliers and noise, high fitting accuracy, and improved performance.**

***Index Terms*— Ellipse fitting, GMM, HGMM, RANSAC, outlier, noise, robust statistic.**

I. Introduction

As ONE of the most common conics, an ellipse represents the perspective projection of a 3D circle that appears in numerous shapes. Therefore, recognizing ellipses from unrecognized data points has a rich history in computer vision and pattern recognition. This problem is particularly important due to its large number of applications in various fields, such as classic computer vision scenarios (including pose estimation [1], [2], camera calibration [3], [4], and face detection [5], [6]) and interdisciplinary areas (including pupil detection for eye tracking [7], [8], touching cell segmentation for biomedical image processing [9]–[11], fetal head measurement [12] and cardiovascular disease diagnosis [13]).

Many studies have explored ellipse fitting over the past several decades by applying two approaches, namely, *least-squares (LS)* based methods and *voting or sampling (VS)* based methods of which LS-based methods, including algebraic and geometric fitting, are the most used. These methods usually work well for clean or simple instances but are highly sensitive to outliers that commonly emerge in practice. Compared with LS-based methods, VS-based methods are more robust against outliers. Some representative VS-based methods include the *Hough transform* (HT) [14] and *random sample consensus* (RANSAC) [15] approaches. However, HT has a relatively large computational cost and storage requirements for the 5D parameter space of an ellipse and is sensitive to the quantization of parameter bins. HT-based methods may even mistakenly fit or miss true ellipses if the quantization is inappropriate. Meanwhile, RANSAC requires multiple iterations to find the optimal solution, but its results cannot be guaranteed to be the same for each time under outlier scenes. Moreover, with the increasing number of outliers, both HT and RANSAC tend to report false ellipses.

To improve the robustness of ellipse fitting, in this work, we propose a novel method called *hierarchical Gaussian mixture models* (HGMM) that fits ellipses from a set of noisy 2D points containing substantial outliers. Our approach is inspired by previous works on point set registration [16] and ellipse detection [17] that use GMM, which has been proven robust for point set registration tasks by minimizing the L_2 norm between two distributions built by two GMMs [16]. Arellano *et al.* [17] adopt the GMM framework for ellipse detection but find that this method is vulnerable to outliers given that the direct transplanting of the L_2 metric cannot distinguish the outliers and inliers effectively, thereby reducing accuracy.

The hierarchical structure of the proposed HGMM is crafted into two layers. First, the outer layer estimates reasonable initial parameters. To this end, a density-based region growing strategy is devised, which effectively circumvents manual deviations or randomness for the initial value setting. Unlike GMM that solely relies on the L_2 norm, we combine distance and density together to create an error metric that is more robust against outliers. Second, on the basis of the results from the outer layer, the inner layer is applied to the whole data to generate the final ellipse. We show that such a hierarchical structure significantly improves the robustness, stability, and accuracy of the GMM framework. The iterative interval of

Manuscript received August 25, 2020; revised February 1, 2021 and March 1, 2021; accepted March 6, 2021. Date of publication March 18, 2021; date of current version March 25, 2021. This work was supported in part by the National Natural Science of Foundation for Outstanding Young Scholars under Grant 12022117, in part by the National Natural Science Foundation of China under Grant 61872354 and Grant 61772523, in part by the Beijing Natural Science Foundation under Grant Z190004 and Grant L182059, in part by the National Key Research and Development Program of China under Grant 2020YFB1708900 and Grant 2019YFB2204104, in part by the Beijing Advanced Discipline Fund under Grant 115200S001, and in part by the Alibaba Group through Alibaba Innovative Research Program. The associate editor coordinating the review of this manuscript and approving it for publication was Dr. Zhao Zhang. *(Corresponding author: Xiaohong Jia.)*

Mingyang Zhao and Xiaohong Jia are with the KLMM, NCMIS, Academy of Mathematics and Systems Science, Chinese Academy of Sciences (CAS), Beijing 100190, China, and also with the School of Mathematical Sciences, University of Chinese Academy of Sciences (UCAS), Beijing 100149, China (e-mail: zhaomingyang@amss.ac.cn; xhjia@amss.ac.cn).

Lubin Fan and Yuan Liang are with the Alibaba Group, Hangzhou 311121, China (e-mail: lubinfan@gmail.com; liangyuan.ly@alibaba-inc.com).

Dong-Ming Yan is with the National Laboratory of Pattern Recognition (NLPR), Institute of Automation, Chinese Academy of Sciences, Beijing 100190, China, and also with the School of Artificial Intelligence, University of Chinese Academy of Sciences, Beijing 100149, China (e-mail: yandongming@gmail.com).

This article has supplementary downloadable material available at https://doi.org/10.1109/TIP.2021.3065799, provided by the authors.

Digital Object Identifier 10.1109/TIP.2021.3065799

the kernel bandwidth is also narrowed down to enhance the efficiency of the fitting process. The main contributions of this paper are as follows:

- A novel ellipse fitting method with remarkable robustness against outliers and noise is proposed, and the iterative interval of the kernel bandwidth is narrowed down.
- A reliable error metric that jointly considers distance and density instead of merely depending on the L_2 norm is introduced.
- The analytical gradients of the objective function are derived to accelerate and stabilize the optimization process.

II. Related Work

In this section, we present the formal definition of ellipse fitting and briefly review the most relevant methods related to our approach. The reader can refer to [18] for a comprehensive study of ellipse fitting.

A. Ellipse Fitting

Definition 1: A conic in 2D Euclidean space is defined by the following implicit second-order polynomial equation:

$$Ax^2 + 2Bxy + Cy^2 + 2Dx + 2Ey + F = 0. \tag{1}$$

Alternatively, this conic can be expressed in a vector form $\Theta^T \mathbf{v}$, where

$$\Theta = [A \quad B \quad C \quad D \quad E \quad F]^T,$$
$$\mathbf{v} = [x^2 \quad 2xy \quad y^2 \quad 2x \quad 2y \quad 1]^T.$$

Equation (1) describes an ellipse if its discriminant

$$B^2 - AC < 0. \tag{2}$$

Given a set of points $C = \{(x_i, y_i) \in \mathbb{R}^2\}_{i=1}^n$ that are sampled on a potential ellipse, possibly with noise or outliers, the goal of ellipse fitting is to extract the ellipse from the points. The existing methods can be generally classified into two those that rely on the least-squares (LS) principle and those that depend on the voting or sampling (VS) technique.

B. Least-Squares Based Methods

LS-based methods aim to solve for the optimal ellipse parameters by minimizing the sum of squared distance between the data points and the ellipse model. Typically, the algebraic and geometric distances are invoked to measure the fitting deviations in a process also known as algebraic and geometric fitting. On the one hand, algebraic fitting aims to minimize

$$J(\Theta) = \sum_{i=1}^{n} \|\Theta^T \mathbf{v_i}\|^2 = \sum_{i=1}^{n} \Theta^T \mathbf{v_i} \mathbf{v_i}^T \Theta = \Theta^T \mathbf{V}^T \mathbf{V} \Theta, \tag{3}$$

where $\mathbf{v_i} = \mathbf{v}(x_i, y_i) = [x_i^2 \quad 2x_i y_i \quad y_i^2 \quad 2x_i \quad 2y_i \quad 1]^T$ is the point vector computed from the input data (x_i, y_i), and $\mathbf{V} = [\mathbf{v_1} \quad \mathbf{v_2} \quad \dots \quad \mathbf{v_n}]^T$ is the *design matrix* constructed from $\{\mathbf{v_i}\}_{i=1}^n$. To avoid scale indeterminacy and trivial solutions, various normalization schemes have been investigated in the past, including

$$\begin{aligned} F = 1, \quad A + C = 1, \\ \| \Theta \|_2 = 1, \quad AC - B^2 = 1. \end{aligned} \tag{4}$$

However, the first three constraints are not ellipse specific, that is, the fitting results may not be an ellipse especially when plenty of outliers exist. Meanwhile, the last constraint, which is proposed by Fitzgibbon *et al.* [19], is ellipse specific and transforms the fitting problem into a generalized eigenvalue system. This approach has since then been called *direct least square fitting* (DLSF). Since its non-iterative and ellipse specific properties, DLSF has been widely used afterwards. Although algebraic fitting methods are computational efficient, they are sensitive to outliers.

Unlike algebraic fitting, geometric fitting estimates ellipses by minimizing the sum of squared orthogonal distance d_i from the observed points (x_i, y_i) to the ellipse [18]:

$$S = \sum_{i=1}^{n} ((x_i - \hat{x}_i)^2 + (y_i - \hat{y}_i)^2) = \sum_{i=1}^{n} d_i^2, \tag{5}$$

where $(\hat{x}_i, \hat{y}_i)$ is the point on the ellipse closest to (x_i, y_i). Compared with algebraic fitting, geometric fitting has higher accuracy but requires iterative optimization due to the non-linear nature of the distance computation. For instance, Ahn *et al.* [20] adopt a direct approach of minimizing the orthogonal distance through iterations. To improve efficiency, several approximations for the exact geometric distance have been proposed, such as the first-order distance approximation (*i.e.*, *Sampson distance*) [21], [22]. Meanwhile, Taubin [23] calculates the gradient of Eq. (1) and transforms the fitting problem as a generalized eigenvalue system. In this way, this approach can also be regarded as an algebraic fitting. However, if the data are corrupted by partial outliers, then this approach may return non-elliptic conics. Prasad *et al.* [24] propose an unconstrained, non-iterative, and LS-based geometric method. However, this method is only suitable for data points that belong to an ellipse. Wu *et al.* [25] recently propose a novel Polar-N-Direction distance that is derived from analyzing the Sampson distance. Nevertheless, the above methods are not suitable for ellipse fitting when a certain number of outliers exists. Moreover, given that geometric fitting involves a non-linear optimization, this process usually requires proper initial guesses and tends to be stuck in the local minima.

According to the Gauss-Markov theorem [26], LS is the best linear unbiased estimator, yet is susceptible to outliers. Therefore, neither algebraic fitting nor geometric fitting can provide reliable results when the data are contaminated by outliers. *Least median squares* (LMS) [27] is later proposed to improve the robustness of LS. The motivation behind this approach is that the optimal solution should embrace the lowest median of squared residuals.

C. Voting or Sampling Based Methods

VS-based methods usually indicate HT [14], [28] and RANSAC [15], [29]. The principle of HT is to perform voting for each point in a 5D parameter space, and the local maxima in the accumulator are selected out as candidate ellipses. However, this method requires large storage and has a high computational complexity, which is computed as $O(N^5)$ [30], where N is the quantized space for each elliptic parameter. To relieve this issue, multiple variants such as probabilistic HT [31], hierarchical HT [32], randomized HT [33], and iterative randomized HT [34], have been proposed. These variants are collectively referred to as the Hough family.

RANSAC adopts an iterative sampling technique. In each iteration, at least five points are randomly sampled, and then

the unknown parameters of an ellipse are solved from these points. However, RANSAC is sensitive to the error bound setting of inliers. In addition, when input data are corrupted by a large portion of outliers, the sampling process needs substantial repetitions and the results cannot be guaranteed equally for each time. Let the outlier percentage among the input data is w, and the probability that at least once the sampled $n = 5$ points are all from the ground truth ellipse is p, then the required sampling number N is equal to

$$N = \frac{\log(1-p)}{\log(1-(1-w)^n)}.$$

For instances, if $w = 0.6$, $p = 0.98$, then $N = 380$, and if $w = 0.8$, then $N = 12,223$ is large enough. Moreover, we have no *prior* of w. Some variants of RANSAC include maximum likelihood estimation consensus (MLESAC) [35], guided-MLESAC [36], and genetic algorithm sample consensus (GASAC) [37].

D. Other Methods

Apart from the above representative methods, many other approaches that depend on different principles are also available. For instance, some of these methods explore the various geometric properties of an ellipse [38], [39] or rely on maximum likelihood and entropy [40], [41]. Innovation sampling [42], sparse combination [43], and heuristic optimization [44], [45] have also been explored for their application in ellipse fitting. However, these methods either ignore the interference of outliers or are incompetent against outliers. Recently, [46] introduces a deep-learning-based method called Ellipse-RCNN, subject to the training datasets, it merely targets for specific objects.

The generalized GMM framework proposed by Arellano *et al.* [17] for ellipse detection is initially used by Jian and Vemuri [16] to perform point set registration. Specifically, they optimize the registration process based on the L_2 norm between two probability distributions. However, directly porting the L_2 norm as the optimal error metric for ellipse fitting is not suitable, because this approach is also susceptible to outliers. To address this issue, we propose a novel distance-density-based error metric that jointly considers the distance and density deviations. We also devise a hierarchical GMM constituted by two layers. Through a density-based region growing step, the outer layer effectively eliminates the initial randomness caused by handcraft. Afterward, the inner layer is applied to the whole data containing outliers to determine the true ellipses. Given the hierarchical structure of this framework, we not only intensively improve its robustness against outliers, but also narrow down the iterative interval of the kernel bandwidth, thereby reducing the computation time and accelerating the fitting process.

III. GMM for Ellipse Fitting

Our method adopts a hierarchical structure that takes GMM as the main ingredient. To make the paper self-contained, we initially review the GMM framework proposed by [17]. GMM is a special case of the non-parametric probability density estimation in the kernel method that is used to approximate the data from an unknown distribution. For instance, given a 2D point set $C = \{\mathbf{x}_j \in \mathbb{R}^2\}_{j=1}^n$, the following probability density function is built:

$$p(\mathbf{x}) = \frac{1}{n}\sum_{j=1}^{n} K_h(\mathbf{x}-\mathbf{x}_j), \tag{6}$$

where $K_h(\mathbf{x}-\mathbf{x}_j)$ is the *kernel function* with the *(kernel) bandwidth* equal to h. $p(\mathbf{x})$ is a Gaussian mixture model if $K_h(\mathbf{x}-\mathbf{x}_j)$ is equal to the following Gaussian kernel $N(\mathbf{x};\boldsymbol{\mu},\boldsymbol{\Sigma})$ defined as

$$N(\mathbf{x};\boldsymbol{\mu},\boldsymbol{\Sigma}) = \frac{1}{2\pi\|\boldsymbol{\Sigma}\|^{1/2}}\exp\{-\frac{1}{2}(\mathbf{x}-\boldsymbol{\mu})^T\boldsymbol{\Sigma}^{-1}(\mathbf{x}-\boldsymbol{\mu})\},$$

where $\boldsymbol{\mu}$ is a 2-dimensional mean vector, $\boldsymbol{\Sigma}$ is a 2×2 covariance matrix, and $\|\boldsymbol{\Sigma}\|$ is the determinant of $\boldsymbol{\Sigma}$. For the given point set C, the data model $f(\mathbf{x})$ is defined as

$$f(\mathbf{x}) = \frac{1}{n}\sum_{j=1}^{n} N(\mathbf{x};\mathbf{x}_j,h^2\mathbf{I}), \tag{7}$$

where $\mathbf{I}$ is a 2×2 identity matrix.

Suppose that we want to fit the given point set by an ellipse with parameter $\boldsymbol{\theta} = (x_0, y_0, a, b, \gamma)$, where (x_0, y_0) is the ellipse center, a, b are the semi-axis length, and γ is the rotational angle with respect to the horizontal axis. Then on the target ellipse, we sample m points $\{\mathbf{u}_i \in \mathbb{R}^2\}_{i=1}^m$ which are defined as

$$\mathbf{u}_i = \begin{pmatrix}\cos\gamma & -\sin\gamma\\ \sin\gamma & \cos\gamma\end{pmatrix}\begin{pmatrix}a\cos\tau_i\\ b\sin\tau_i\end{pmatrix}+\begin{pmatrix}x_0\\ y_0\end{pmatrix}, \tag{8}$$

with τ evenly sampled from $[0, 2\pi)$. Then the ellipse model $g(\mathbf{x}|\boldsymbol{\theta})$ for the target ellipse is built as

$$g(\mathbf{x}|\boldsymbol{\theta}) = \sum_{i=1}^{m} w_i N(\mathbf{x};\boldsymbol{\mu}_i,\boldsymbol{\Sigma}_i), \tag{9}$$

where the mean $\boldsymbol{\mu}_i$ and covariance matrix $\boldsymbol{\Sigma}_i$ are defined as

$$\boldsymbol{\mu}_i = \frac{\mathbf{u}_i+\mathbf{u}_{i+1}}{2}, \quad \boldsymbol{\Sigma}_i = \mathbf{Q}_i^T\boldsymbol{\Lambda}_i\mathbf{Q}_i.$$

$\mathbf{Q}_i = [\mathbf{n}_{1i}|\mathbf{n}_{2i}]$ is composed of two orthogonal unit vectors $\mathbf{n}_{1i}$ and $\mathbf{n}_{2i}$,

$$\mathbf{n}_{2i} = \frac{\mathbf{u}_i-\mathbf{u}_{i+1}}{||\mathbf{u}_i-\mathbf{u}_{i+1}||_2} = [n_{2i}(x), n_{2i}(y)]^T,$$
$$\mathbf{n}_{1i} = \mathbf{R}\mathbf{n}_{2i} = [-n_{2i}(y), n_{2i}(x)]^T.$$

$\mathbf{R} = \begin{pmatrix}\cos\alpha & -\sin\alpha\\ \sin\alpha & \cos\alpha\end{pmatrix}$ is the rotation matrix with the angle $\alpha = \pi/2$. $\mathbf{n}_{1i}$ and $\mathbf{n}_{2i}$ can be seen as approximations of the normal and tangent vectors of the ellipse at point $\boldsymbol{\mu}_i$. $\boldsymbol{\Lambda}_i$ is a diagonal matrix

$$\begin{pmatrix}h^2 & 0\\ 0 & h_i^2\end{pmatrix},$$

with $h_i = ||\mathbf{u}_i-\mathbf{u}_{i+1}||_2$. The weights w_i of $g(\mathbf{x}|\boldsymbol{\theta})$ satisfy

$$1 = \int_{-\infty}^{+\infty} g(\mathbf{x}|\boldsymbol{\theta})d\mathbf{x} = \sum_{i=1}^{m} w_i\int_{-\infty}^{+\infty} N(\mathbf{x};\boldsymbol{\mu}_i,\boldsymbol{\Sigma}_i)d\mathbf{x} = \sum_{i=1}^{m} w_i,$$

and are set as $\frac{h_i}{\sum_{i=1}^m h_i}$. To capture the shape of an ellipse, the number m in $g(\mathbf{x}|\boldsymbol{\theta})$ is set to 20 [17]. An illustration of the ellipse model $g(\mathbf{x}|\boldsymbol{\theta})$ is presented in Fig 1.

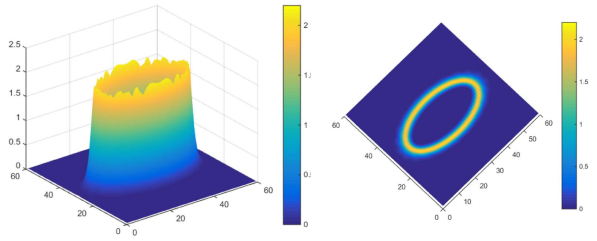

Fig. 1. Perspective visualization and bird's-eye view of the ellipse model $g(\mathbf{x}|\boldsymbol{\theta})$.

The difference between $f(\mathbf{x})$ and $g(\mathbf{x}|\boldsymbol{\theta})$ is evaluated by

$$L_2(\boldsymbol{\theta}) = \|f(\mathbf{x}) - g(\mathbf{x}|\boldsymbol{\theta})\|_2. \tag{10}$$

Therefore, the optimal ellipse parameter $\boldsymbol{\theta}$ is acquired at

$$\hat{\boldsymbol{\theta}} = \arg\min_{\boldsymbol{\theta}} \|f(\mathbf{x}) - g(\mathbf{x}|\boldsymbol{\theta})\|_2. \tag{11}$$

Eq. (10) can be rewritten as

$$\|f(\mathbf{x}) - g(\mathbf{x}|\boldsymbol{\theta})\|_2^2 = \|f(\mathbf{x})\|_2^2 + \|g(\mathbf{x}|\boldsymbol{\theta})\|_2^2 - 2 < f(\mathbf{x})|g(\mathbf{x}|\boldsymbol{\theta}) >,$$

based on the inner product of Gaussian distributions,

$$< N(\boldsymbol{\mu}_1, \boldsymbol{\Sigma}_1)|N(\boldsymbol{\mu}_2, \boldsymbol{\Sigma}_2) >= N(\mathbf{0}; \boldsymbol{\mu}_1 - \boldsymbol{\mu}_2, \boldsymbol{\Sigma}_1 + \boldsymbol{\Sigma}_2),$$

we obtain

$$\|g(\mathbf{x}|\boldsymbol{\theta})\|_2^2 = \sum_{i=1}^{m}\sum_{k=1}^{m} w_i w_k N(\mathbf{0}; \boldsymbol{\mu}_i - \boldsymbol{\mu}_k, \boldsymbol{\Sigma}_i + \boldsymbol{\Sigma}_k),$$

and

$$< f(\mathbf{x})|g(\mathbf{x}|\boldsymbol{\theta}) >= \frac{1}{n}\sum_{j=1}^{n}\sum_{i=1}^{m} w_i N(\mathbf{0}; \mathbf{x}_j - \boldsymbol{\mu}_i, h^2\mathbf{I} + \boldsymbol{\Sigma}_i).$$

For the point set registration problem, Eq. (10) evaluates the discrepancy between the two distributions through the L_2 norm. However, for ellipse fitting, when the input data set is contaminated by substantial outliers, there exists major differences between the clean ellipse model $g(\mathbf{x}|\boldsymbol{\theta})$ and the data model $f(\mathbf{x})$. Thereby, merely relying on the L_2 norm is not sufficient to get the correct ellipses. As is presented in Fig. 2, the result ellipse by GMM is far away from the correct one. To tackle this problem, we propose the method HGMM in the following sections.

IV. Distance-Density-Based Error Metric

Before presenting the whole HGMM framework, we propose a novel metric that combines the distance and density for deciding the optimal ellipse apart from evaluating the L_2 norm. The proposed distance-density-based error metric follows two criteria [30]:

(1) The data points on or near the model (inliers) should be as many as possible, and
(2) the residual of inliers should be as small as possible.

Definition 2: Given a point set $C = \{\mathbf{x}_j \in \mathbb{R}^2\}_{j=1}^n$ and an ellipse with parameter $\boldsymbol{\theta}$, the proposed error metric is

$$E(\boldsymbol{\theta}) = \frac{\sum_{j=1}^n d_{\boldsymbol{\theta}}(\mathbf{x}_j)}{\exp\{\sum_j^n \mathbb{1}(d_j^2 < T^2) f(\mathbf{x}_j)\}}, \tag{12}$$

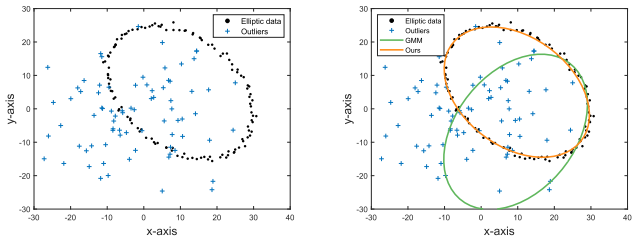

Fig. 2. Left: The elliptic data are contaminated by outliers. Right: The fitting results obtained by GMM and the proposed method.

Algorithm 1 Distance-Density-Based Ellipse Fitting

Input: Point set C, Initial ellipse parameter $\boldsymbol{\theta}^{(0)}$, Iterative interval of bandwidth $[h_{max}, h_{min}]$, Inlier threshold T.
Output: Optimal ellipse parameter $\hat{\boldsymbol{\theta}}$.

```
Initialize h ← h_max, θ̂ ← θ^(0), and E ← ∞;
Construct the ellipse model g(x|θ) and data model f(x);
Calculate f(x_i) for each point x_i ∈ C;
while h ≥ h_min do
    θ̂ ← arg min_θ ‖f(x) − g(x|θ)‖_2;
    if E(θ̂) < E then
        E ← E(θ̂);
        θ̂ ← θ̂;
    end if
    h ← 0.8 × h;
end while
Output θ̂;
```

where $d_{\boldsymbol{\theta}}(\mathbf{x}_j)$ is the distance from the select points $\mathbf{x}_j$ to the ellipse $\boldsymbol{\theta}$ (using $\boldsymbol{\theta}$ to represent the ellipse)

$$d_{\boldsymbol{\theta}}(\mathbf{x}_j) = \begin{cases} d_j^2, & d_j^2 < T^2 \\ +\infty, & d_j^2 \geq T^2, \end{cases}$$

and $\mathbb{1} : \mathbb{R} \to \{0, 1\}$ is the indicator function, and T is the inlier threshold.

Given the lack of an explicit point-to-ellipse distance formula,[1] we adopt the following approximate formula [47] that holds for canonical ellipses (centered at the origin and aligned with the axes) for the distance computation:

$$d_j = \begin{cases} r(1 - \sqrt{(x_j/a)^2 + (y_j/b)^2}), & \mathbf{x}_j \text{ is inside } \boldsymbol{\theta} \\ \sqrt{x_j^2 + y_j^2}(1 - \dfrac{1}{\sqrt{(x_j/a)^2 + (y_j/b)^2}}), & \mathbf{x}_j \text{ is outside } \boldsymbol{\theta} \end{cases}$$

where $r = \min(a, b)$. We transform the fitted ellipse $\boldsymbol{\theta}$ into a canonical form to utilize this formula.

Remark: The optimal ellipse solution $\hat{\boldsymbol{\theta}}$ is acquired at the minimal of $E(\boldsymbol{\theta})$.

Minimizing Eq. (12) requires its numerator, which characterizes Criterion (2) on the total distance of inliers, to be the smallest and requires its denominator, which characterizes Criterion (1) on the total density of inliers, to be the largest. Therefore, the whole effect of Eq. (12) is to force the fitting tending to inliers thus the minimal $E(\boldsymbol{\theta})$ corresponds to the optimal ellipse solution $\hat{\boldsymbol{\theta}}$.

[1]Calculating the exact Euclidean distance from a point to an ellipse requires solving a quartic equation. Additional details on the exact computation and approximate computation of [47] are presented in the supplemental material.

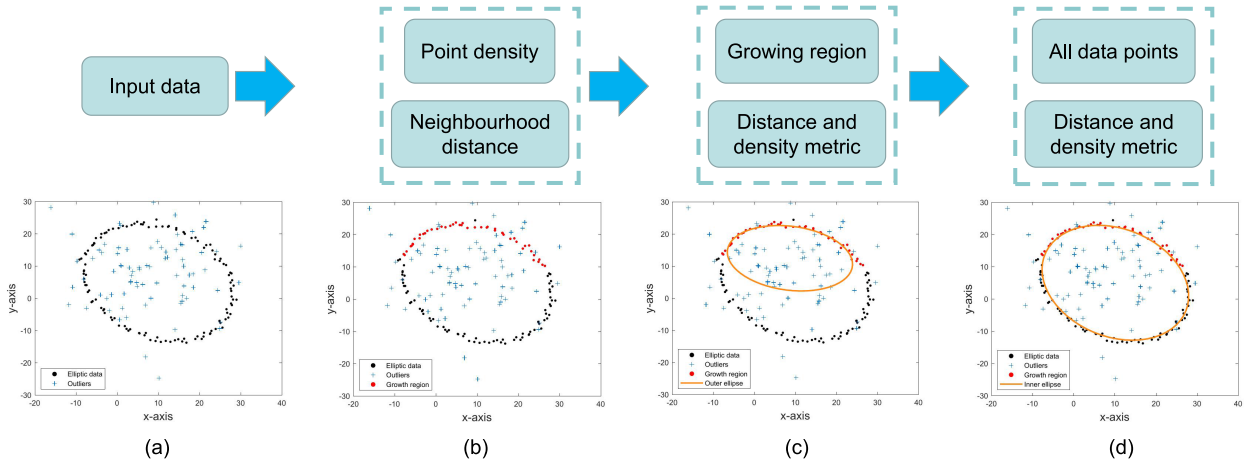

Fig. 3. Top: The pipeline of the proposed robust ellipse fitting method. Bottom: Illustrative description of the proposed method. (a) Input data. (b) The growing region based on the density and distance computation. (c) The ellipse fitted by the outer layer. (d) The ellipse fitted by the inner layer.

In practice, we adopt a simulated annealing method by changing the h provided by users in Eq. (11) from its maximum to minimum to solve for the optimal solution $\hat{\boldsymbol{\theta}}$.

Definition 3: The iterative interval of the bandwidth is defined as $[h_{max}, h_{min}]$, *which descends from the maximum* h_{max} *to the minimum* h_{min}. *In the iterative process, the same geometric iteration rate* $\beta = 0.8$ *is utilized.*

Under each bandwidth, the gradient descent algorithm with the analytical gradient provided in the supplemental material is used to minimize $L_2(\boldsymbol{\theta})$. The proposed algorithm is presented in Algorithm 1.

V. HGMM for Ellipse Fitting

In this section, we present the complete HGMM framework as shown in Fig. 3, along with an illustrative description. Given that the initial value $\boldsymbol{\theta}^{(0)}$ plays a key role in determining the correct ellipses, we create a hierarchical structure containing two layers to address this problem. Under each layer, we search for a proper initial value for $\boldsymbol{\theta}^{(0)}$ prior to fitting. Generally speaking, for the input data given in Fig. 3(a), we first adopt region growing strategy combining point density and neighborhood distance together to decide the initial value for the outer fitting, as shown in Fig. 3(b). Then the outer fitting is implemented for the growing region to attain the first ellipse, which is presented in Fig. 3(c). Based on the outer fitting result, the inner fitting is applied to the entire data involving outliers to further improve the fitting accuracy. The final ellipse in Fig. 3(d) shows that our proposed method is robust against outliers. Detailed descriptions are presented in the following sections.

A. Density-Based Region Growing Method

Based on the observation that the points on or near ellipses have higher and comparable density than the outliers, we devise a density-based region growing strategy to remove the outliers. Specifically, for the given input point set $C = \{\mathbf{x}_i \in \mathbb{R}^2\}_{i=1}^n$, such as the case in Fig. 3(a), we calculate the density $\rho(\mathbf{x}_i)$ for each point $\mathbf{x}_i$ by letting $\mathbf{x} = \mathbf{x}_i$ in the data model $f(\mathbf{x})$, and choose the point with the largest density $\rho_0 = \max_{i=1}^n \rho(\mathbf{x}_i)$ as the initial point $\mathbf{x}_0$ of the growing region R. Afterward, we rely on the following definition to expand R:

Definition 4: A point $\mathbf{x}_i \in C$ *can be grouped into the neighborhood of* $\mathbf{x}_0$, *that is,* $\mathrm{NEps}(\mathbf{x}_0)$, *if it lies within the sphere* $S_\epsilon(\mathbf{x}_0)$ *and has a comparable density with* ρ_0*:*

$$\mathrm{NEps}(\mathbf{x}_0) = \{\mathbf{x}_i \in C | \parallel \mathbf{x}_i - \mathbf{x}_0 \parallel_2 \leq \epsilon \cap \frac{\rho(\mathbf{x}_i)}{\rho_0} \geq \tau\},$$

where τ *is the density tolerance with respect to* ρ_0 *and is typically fixed to 0.6.*

Afterward, we add $\mathrm{NEps}(\mathbf{x}_0)$ to R and update the start point $\mathbf{x}_0$ by one of the farthest points in $\mathrm{NEps}(\mathbf{x}_0)$ from $\mathbf{x}_0$, along with the update of ρ_0. This process is repeated until the point number $|R|$ reaches the given threshold N. If $|R|$ fails to reach N, then R is seen as outliers and is removed from C. For the input data in Fig. 3(a), its growing region is presented in Fig. 3(b).

B. Fitting in the Outer and Inner Layers

For the valid region R, we utilize Algorithm 1 to fit the points in R with the initial value $\boldsymbol{\theta}^{(0)} = (x_0, y_0, 1, 1, 0)$. Here, (x_0, y_0) is the average of all points in R. This process is the outer fitting step, and the corresponding fitting result is presented in Fig. 3(c). After obtaining $\boldsymbol{\theta}^{(1)}$ from the outer layer, the inner layer (*i.e.*, Algorithm 1) is rerun by taking $\boldsymbol{\theta}^{(1)}$ as its initial value for the whole point set C containing outliers to authentically determine the correct ellipse. The inner fitting result is presented in Fig. 3(d), which successfully fits the true ellipse. The iterative intervals of bandwidth in the outer and inner layers are set as $[h_{maxo}, h_{mino}]$ and $[h_{maxi}, h_{mini}]$, respectively. The above procedures are summarized in Algorithm 2.

Given that most points in R come from the true ellipse, reasonable initial values can be provided for the outer layer, thereby guaranteeing the optimal $\boldsymbol{\theta}^{(1)}$ that subsequently becomes the initial value for the inner layer. Based on $\boldsymbol{\theta}^{(1)}$, the final ellipse is determined through a very narrow bandwidth. Owing to its hierarchical structure, compared with GMM, the iterative interval of bandwidth is effectively narrowed down, thereby accelerating the fitting process.

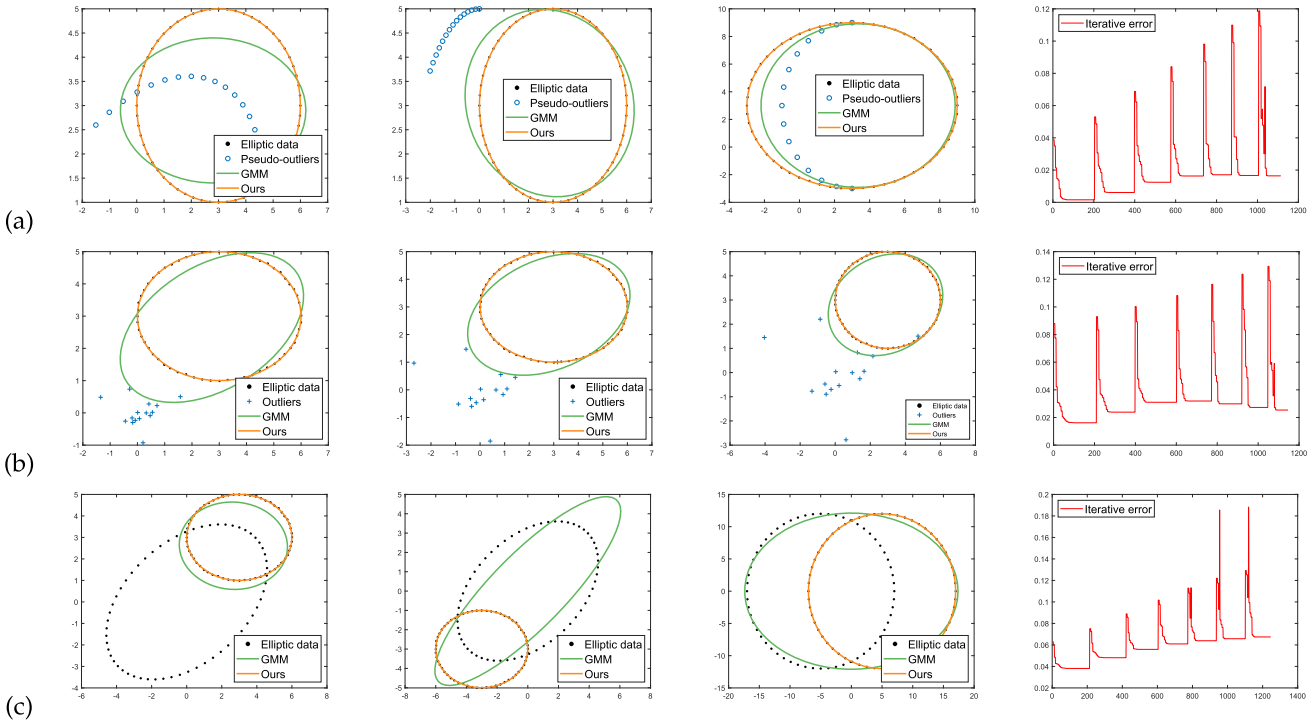

Fig. 4. Ellipse fitting comparisons between GMM and the proposed method. The first to third rows show the cases of pseudo-outliers, random outliers, and two ellipses. The last column shows the corresponding L_2 error of GMM for the first column. Our distance-density-based method successfully fits all correct ellipses.

VI. Experimental Evaluation and Discussions

In this section, extensive experiments that utilize synthetic data and real-world images are conducted to demonstrate the accuracy and robustness of the proposed method compared with the representative state-of-the-art methods. All experiments are conducted with Matlab R2014b on a PC with 4GB RAM and a 3.6 GHz Intel CPU.

A. Comparison With GMM

To verify the effectiveness of the proposed metric $E(\boldsymbol{\theta})$ (Section IV), we compare our algorithm (Algorithm 1) with the primary GMM-based ellipse fitting [17] by conducting three experiments (*i.e.*, *pseudo-outliers*, *outliers*, and *two ellipses*). For each experiment, three different cases are tested to attain representative results as shown in Fig. 4. For the sake of fairness, Algorithm 1 and GMM share the same parameter settings and bandwidth interval (*i.e.*, $h \in [0.9, 0.2]$) in all tests.

For the pseudo-outliers case, a complete ellipse is randomly generated and associated with a quarter ellipse at different locations to simulate various interferences. The initial guess $\boldsymbol{\theta}^{(0)}$ for both methods is equal to $(x_0, y_0, 1, 1, 0)$, where (x_0, y_0) is the center of the complete ellipse. The fitting results are presented in Fig. 4(a). We can see from the figure that GMM is affected by pseudo-outliers and loses three correct ellipses. To illustrate the optimization process of GMM, we also report the L_2 iterative error in the fourth column for the first case. We observe that the optimal ellipse $\hat{\boldsymbol{\theta}}$ of GMM is obtained when $h = 0.9$ with a minimal L_2 error of 1.5586×10^{-3}. However, the correct ellipse is fitted at $h = 0.24$ with an L_2 error of 1.64×10^{-2}, thereby suggesting that the minimal L_2 error does not correspond to the optimal ellipse under the existence of pseudo-outliers. By contrast, our distance-density-based method successfully fits three correct ellipses under different interferences. Therefore, our proposed metric is more robust against pseudo-outliers compared with GMM.

In the second test, we contaminate the ellipse by 15 random outliers from a Gaussian distribution with zero mean and standard deviations (σ): 5%, 100%, and 150%, as shown in Fig. 4(b). As observed, the ellipses fitted by GMM under the minimal L_2 error deviate from the correct ellipses, yet our distance-density-based method fits all the ellipses. The last experiment is conducted to simulate the multiple ellipse detection by using two intersecting ellipses as shown in Fig. 4(c). Although the initial location provided for GMM has been designated as one of the true ellipses for the first two cases, GMM still misses the correct ellipses. By contrast, our method successfully fits one of the correct ellipses. It is also interesting to see what will happen if two same ellipses are available. Therefore, we generate a symmetric configuration of two ellipses as shown in the third image and set the initial location (x_0, y_0) at the symmetric center $(0, 0)$. Note that our method still performs well and fits one of the correct ellipses. Meanwhile, GMM, which is only based on the L_2 norm, generates major deviations.

Experimental results indicate that under the outlier contamination, merely relying on the L_2 metric for ellipse fitting is not sufficient or reliable because the data distribution $f(\mathbf{x})$ greatly changes compared with the ellipse model $g(\mathbf{x}|\boldsymbol{\theta})$. By reconsidering the model fitting criteria and designing a novel error metric, our method successfully fits all the correct ellipses.

Algorithm 2 HGMM for Ellipse Fitting

Input: Point set C, Point number in growing region N, Neighborhood radius ϵ, Iterative interval of bandwidth in outer and inner fitting $[h_{maxo}, h_{mino}]$, $[h_{maxi}, h_{mini}]$, Inlier threshold T.

Output: Optimal ellipse parameter $\hat{\boldsymbol{\theta}}$.

Calculate $\rho(\mathbf{x}_i)$ for each point $\mathbf{x}_i \in C$ by $f(\mathbf{x})$;
Find the point $\mathbf{x}_0 \in C$ with the maximal density ρ_0;
$R \leftarrow \emptyset$, flag $\leftarrow$ true;
while flag **do** ▷ density-based region growing
  $\text{NEps}(\mathbf{x}_0) \leftarrow \{\mathbf{x}_i \in C | \parallel \mathbf{x}_i - \mathbf{x}_0 \parallel_2 \leq \epsilon \cap \frac{\rho(\mathbf{x}_i)}{\rho_0} \geq 0.6\}$;
  $R \leftarrow R \cup \text{NEps}(\mathbf{x}_0)$;
  Remove $\text{NEps}(\mathbf{x}_0)$ from C;
  $\mathbf{x}_0 \leftarrow \max_{\mathbf{x}_i \in \text{NEps}(\mathbf{x}_0)} \parallel \mathbf{x}_i - \mathbf{x}_0 \parallel_2$, $\rho_0 \leftarrow f(\mathbf{x}_0)$;
  if $\text{NEps}(\mathbf{x}_0)$ is empty **then**
    flag $\leftarrow$ false;
    Remove R from C;
  else if $|R| \geq N$ **then** ▷ fitting in outer layer
    flag $\leftarrow$ false;
    Initialize (x_0, y_0) by the center of R;
    Initialize $\boldsymbol{\theta}^{(0)} \leftarrow (x_0, y_0, 1, 1, 0)$;
    Estimate $\boldsymbol{\theta}^{(1)}$ by Alg. 1 using $(R, h_{maxo}, h_{mino}, \boldsymbol{\theta}^{(0)}, T)$;
    Calculate the aspect ratio e of $\boldsymbol{\theta}^{(1)}$;
    if $e < \frac{1}{5}$ **then** ▷ inner layer
      $\boldsymbol{\theta}^{(1)} = (\boldsymbol{\theta}^{(1)}(1), \boldsymbol{\theta}^{(1)}(2), 1, 1, 0)$;
    end if
    Estimate $\hat{\boldsymbol{\theta}}$ by Alg. 1 using $(C, h_{maxi}, h_{mini}, \boldsymbol{\theta}^{(1)}, T)$;
  else continue;
  end if
end while
Output $\hat{\boldsymbol{\theta}}$;

B. Quantitative Evaluations

To comprehensively assess its accuracy and robustness, we compare our proposed method with eight representative or recently proposed ellipse fitting methods from three categories, including DLSF [19], Taubin [23], Ahn [20], Prasad [24], Wu [25], RANSAC [15], LMS [27], and GMM [17], among which DLSF and Taubin are algebraic fitting methods, Ahn, Prasad, and Wu are geometric fitting methods, and RANSAC, LMS, and GMM are robust methods. To quantitatively evaluate the performance of these algorithms, we measure the ellipse parameters (the center (x_0, y_0), the length of semi-axis a and b, and the rotation angle γ) by the following criteria:

$$\begin{cases} \text{AD}(\hat{x}_0, \hat{y}_0) = \frac{1}{s}\sum_{i=1}^{s}\sqrt{(\hat{x}_i - x_0)^2 + (\hat{y}_i - y_0)^2}, \\ \text{A}(\hat{a}) = \frac{1}{s}\sum_{i=1}^{s}\hat{a}_i, \text{A}(\hat{b}) = \frac{1}{s}\sum_{i=1}^{s}\hat{b}_i, \text{A}(\hat{\gamma}) = \frac{1}{s}\sum_{i=1}^{s}\hat{\gamma}_i. \end{cases}$$

where $(\hat{x}_i, \hat{y}_i, \hat{a}_i, \hat{b}_i, \hat{\gamma}_i)$ is the estimated elliptic parameter for the i^{th} fitting, and s is the fitting times.

C. Numerical Experiments

1) Implementation Details: We first discuss the parameters used in the following experiments. For the proposed method, the iterative interval of the bandwidth is set as $[h_{maxo}, h_{mino}] = [4, 3]$ and $[h_{maxi}, h_{mini}] = [0.9, 0.7]$ with $\beta = 0.8$. For the neighborhood radius ϵ, to capture more inliers, we set $\epsilon = 10$ in all experiments. For the inlier tolerance T, to depress noise influence, we equate it to three. The last parameter N controlling the point number in the growing region is related to the inlier percentage. When the portion of outliers is small, a small N is adequate, while for heavy outliers, we can choose a slightly larger N to ensure better performance. In practice, we leave N as a parameter that can be freely tuned by users. For the primary GMM, we adopt the parameters used in [17] and set $[h_{max}, h_{min}] = [0.9, 0.2]$ with $\beta = 0.8$ in all experiments. Compared with that in GMM, the iterative interval of the bandwidth in our method has been significantly narrowed down. Nevertheless, experiments show that our method is more robust against outliers and attains more accurate fitting results than GMM. Meanwhile, the parameters of other robust methods are set following the suggestions of previous authors. For instance, the maximum iteration number of RANSAC is set to 5000 and its corresponding inlier distance is equal to $\sqrt{0.38}\frac{\sqrt{2}}{\frac{1}{n}\sum_{j=1}^{n}\sqrt{x_j^2+y_j^2}}$, where $\{(x_j, y_j) \in \mathbb{R}^2\}_{j=1}^{n}$ is the input point set. For LMS, the iterative number is set to $\frac{n}{15}$.

2) Noise and Occlusion Disturbance: We first evaluate the performance of different methods in terms of noise. First of all, we add Gaussian noise with zero mean and $\sigma \in \{10\%, 50\%, 100\%, 150\%, 180\%, 200\%\}$ to a randomly generated ellipse $(0, 0, 15, 20, \frac{\pi}{4})$ containing 120 points, besides, we add 10% outliers to the ellipse. Under each noise level σ, we implement $s = 200$ fittings to attain the statistically representative results.

The fitting results are reported in Tables I and II. Table I shows that the overall algebraic and geometric fitting methods have a more stable center deviation $\text{AD}(\hat{x}_0, \hat{y}_0)$ than the robust methods. However, our method achieves a lower $\text{AD}(\hat{x}_0, \hat{y}_0)$ than others under different noise levels, thereby indicating that it has the most precise location estimation. Both RANSAC and LMS tend to produce large center deviations with increasing noise, whereas GMM has the worst deviations that are more than 100 times larger than our method even at $\sigma = 10\%$. In terms of the rotation angle, except for Prasad and LMS, all methods report reliable estimations. Moreover, RANSAC and our method attain the best estimation with our method showing better stability than RANSAC. The semi-axis estimation reported in Table II suggests that Ahn and Wu return a semi-minor axis that is much lower than the ground truth, whereas GMM returns a much larger semi-major axis. By contrast, the other methods report a preferable accuracy with sub-pixel deviations.

To get more insights, we further calculate the *mean squared error* $\text{MSE}(\hat{\xi}) = \frac{1}{s}\sum_{i=1}^{s}(\hat{\xi}_i - \bar{\xi})^2$ for the estimated parameter $\hat{\xi}_i$ (*i.e.*, $(\hat{x}_i, \hat{y}_i), \hat{a}_i, \hat{b}_i, \hat{\gamma}_i$), where $\bar{\xi}$ represents the average. The MSE of each method is presented in Fig. 5.

From which, we can see that GMM has the largest errors for all parameter estimations. Although algebraic fitting and geometric fitting keep more stable than RANSAC and ours, they have much more deviations. Compared with RANSAC, our method is of a little fluctuation, but it still lies in the quite small error scope. A comparison example is presented in Fig. 6.

After the noise test, we remove quarter of the ellipse and set $\sigma = 50\%$ to evaluate the fitting performance of different

TABLE I

FITTING RESULTS OF THE CENTER AND ROTATION ANGLE UNDER DIFFERENT NOISE LEVELS (%)

Methods		AD($\hat{x}_0, \hat{y}_0$)						A($\hat{\gamma}$)					
		10	50	100	150	180	200	10	50	100	150	180	200
Algebraic	DLSF [19]	0.572	0.579	0.596	0.622	0.641	0.655	0.78	0.781	0.782	0.791	0.792	0.793
	Taubin [23]	0.596	0.604	0.624	0.656	0.680	0.698	0.792	0.793	0.795	0.789	0.794	0.798
Geometric	Ahn [20]	0.624	0.624	0.641	0.676	0.697	0.712	0.847	0.786	0.789	0.79	0.79	0.79
	Prasad [24]	0.623	0.632	0.657	0.697	0.727	0.751	1.052	1.059	1.076	1.103	1.121	1.134
	Wu [25]	0.747	0.743	0.763	0.787	0.805	0.820	0.782	0.782	0.785	0.789	0.79	0.791
Robust	RANSAC [15]	0.258	0.282	0.327	0.414	0.511	1.112	0.784	0.783	0.782	0.781	0.782	0.787
	LMS [27]	0.521	0.549	0.751	0.935	1.113	1.083	0.726	0.723	0.686	0.664	0.653	0.639
	GMM [17]	5.961	4.718	5.5	5.212	6.747	7.022	0.792	0.773	0.786	0.782	0.82	0.768
	HGMM(Ours)	0.021	0.085	0.276	0.408	0.524	0.637	0.785	0.786	0.786	0.789	0.789	0.789

TABLE II

FITTING RESULTS OF THE SEMI-AXIS LENGTH UNDER DIFFERENT NOISE LEVELS (%)

Methods		A($\hat{a}$)						A($\hat{b}$)					
		10	50	100	150	180	200	10	50	100	150	180	200
Algebraic	DLSF [19]	14.877	14.898	14.954	15.044	15.112	15.163	19.116	19.116	19.125	19.148	19.17	19.188
	Taubin [23]	14.514	14.525	14.552	14.593	14.623	14.645	19.698	19.71	19.764	19.862	19.944	20.01
Geometric	Ahn [20]	13.62	13.62	13.623	13.626	13.628	13.629	20.363	20.373	20.419	20.509	20.583	20.643
	Prasad [24]	14.26	14.26	14.254	14.24	14.227	14.217	20.477	20.527	20.692	20.979	21.217	21.405
	Wu [25]	13.738	13.74	13.752	13.759	13.762	13.765	19.971	19.983	20.017	20.096	20.16	20.211
Robust	RANSAC [15]	15.089	15.132	15.188	15.26	15.341	15.728	19.856	19.854	19.857	19.825	19.808	19.746
	LMS [27]	14.673	14.582	14.66	14.649	14.739	14.672	19.872	19.818	20.012	20.11	20.179	20.066
	GMM [17]	17.977	15.93	16.827	14.879	15.748	15.172	25.143	24.081	23.481	20.28	21.062	21.14
	HGMM(Ours)	14.776	14.762	14.672	14.675	14.697	14.689	19.807	19.784	19.695	19.709	19.714	19.772

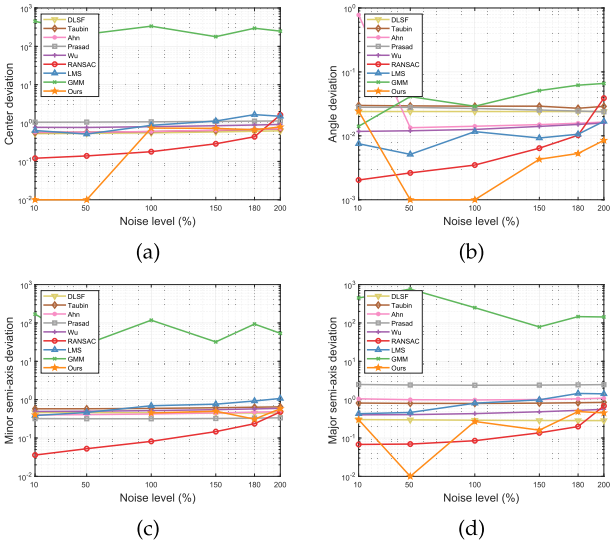

Fig. 5. MSE of different methods under different noise levels (%). (a) Center deviation; (b) angle deviation; (c) minor semi-axis deviation; and (d) major semi-axis deviation.

methods under occlusion. The result is reported in Table III. Our method still has the lowest center deviation among all methods, and both of its semi-axis and rotation angle are very close to the optimal solution. Meanwhile, the LS-based methods produce more center deviations than the robust methods and, except for Taubin, report major angle deviations. LMS also reports evident angle deviations.

3) Outlier Disturbance: Apart from noise tests, we further conduct experiments to evaluate the robustness of our proposed method against outliers. Given that LS-based methods are sensitive to outliers, only four robust methods are compared

TABLE III

FITTING RESULTS OF DIFFERENT METHODS UNDER OCCLUSION

Methods		AD($\hat{x}_0, \hat{y}_0$)	A($\hat{a}$)	A($\hat{b}$)	A($\hat{\gamma}$)
Algebaric	DLSF [19]	1.035	14.746	19.280	0.684
	Taubin [23]	1.329	14.697	20.430	0.783
Geometric	Ahn [20]	1.445	13.911	20.362	0.681
	Prasad [24]	1.693	14.961	21.711	0.997
	Wu [25]	1.229	13.969	19.818	0.676
Robust	RANSAC [15]	0.707	15.203	19.719	0.783
	LMS [27]	0.791	14.539	19.652	0.684
	GMM [17]	0.217	14.717	19.748	0.788
	HGMM(Ours)	0.147	14.756	19.812	0.793

in this experiment. For the previous ellipse $(0, 0, 15, 20, \frac{\pi}{4})$ containing 120 points with $\sigma = 50\%$, we gradually add outliers from 20% to 60%, and implement 200 tests under each outlier level.

The fitting results for different methods are reported in Table IV. RANSAC and our method attain the smallest center deviations, whereas LMS and GMM return large deviations. In terms of rotation angle, except for LMS that obtains large deviations, all the other methods achieve satisfactory results. However, our proposed method achieves the best estimation. For the minor semi-axis, as the outliers increase, the estimation results of RANSAC and GMM tend to be larger and show greater deviations than LMS and our method. For the major semi-axis, LMS reports significant deviations as the outliers increase. Therefore, LMS and GMM may not report reliable results when partial outliers are available. By contrast, RANSAC and our method are highly robust against outliers and are capable of keeping reliable estimations even at 60% outliers.

We further report the MSE for each method in Fig. 7. The proposed method achieves the smallest MSE among all robust methods. Specifically, our method keeps the 10^{-2} center deviation when the outliers are no greater than 50% and

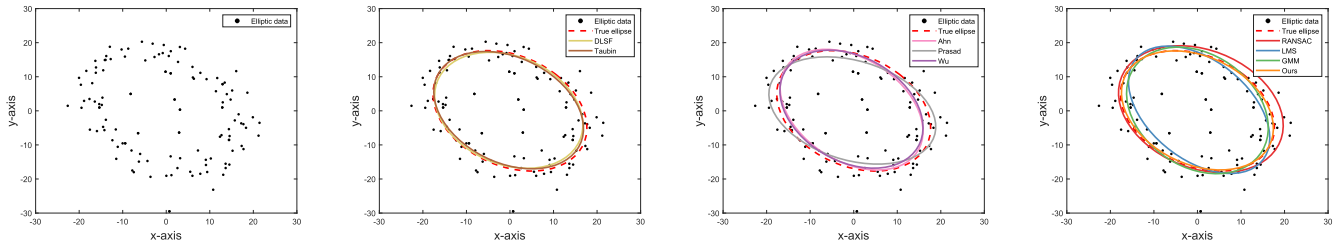

Fig. 6. Comparison of different methods in terms of noise. (a) Input data with $\sigma = 200\%$. (b)-(d) Fitting results attained by algebraic, geometric, and robust methods, respectively.

TABLE IV
FITTING RESULTS OF ELLIPTIC PARAMETERS UNDER DIFFERENT OUTLIERS (%)

Methods	AD$(\hat{x}_0, \hat{y}_0)$					A$(\hat{\gamma})$					A$(\hat{a})$					A$(\hat{b})$				
	20	30	40	50	60	20	30	40	50	60	20	30	40	50	60	20	30	40	50	60
RANSAC [15]	0.07	0.09	0.095	0.318	0.474	0.793	0.78	0.784	0.777	0.796	15.194	15.282	15.249	15.882	16.260	19.89	19.89	19.86	20.15	20.705
LMS [27]	0.681	1.402	1.568	1.679	3.877	0.544	0.527	0.489	0.574	0.546	15.361	15.364	15.094	15.126	14.553	23.841	29.055	32.957	36.09	53.159
GMM [17]	4.181	5.239	4.883	4.760	5.817	0.79	0.778	0.791	0.796	0.79	15.53	14.704	15.670	15.680	17.417	21.54	20.476	20.913	20.853	22.158
GMM+A1	0.087	0.258	0.212	0.429	0.814	0.787	0.776	0.785	0.779	0.774	14.738	14.609	14.773	14.889	14.79	19.765	21.681	19.891	19.884	19.945
SAREfit [48]	1.086	2.732	1.434	3.782	4.344	0.598	0.443	0.193	0.074	1.222	14.846	16.002	18.201	19.611	20.605	21.319	20.749	22.969	24.788	26.22
HGMM(Ours)-A1	0.842	1.214	0.526	0.75	0.924	0.783	0.796	0.792	0.795	0.784	22.494	15.22	14.529	15.049	14.875	27.482	20.507	20.04	20.275	20.45
HGMM(Ours)	0.08	0.087	0.135	0.04	0.54	0.786	0.786	0.782	0.783	0.786	14.76	14.769	14.741	14.801	14.658	19.78	19.78	19.75	19.80	19.617

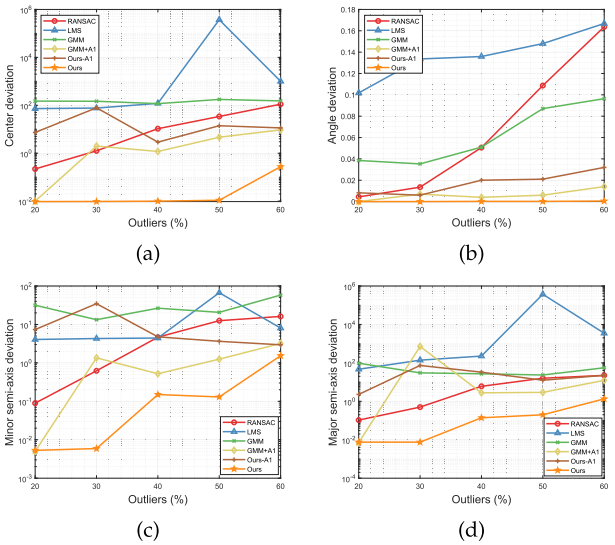

Fig. 7. MSE of different methods under different outliers (%). (a) Center deviation; (b) angle deviation; (c) minor semi-axis deviation; and (d) major semi-axis deviation.

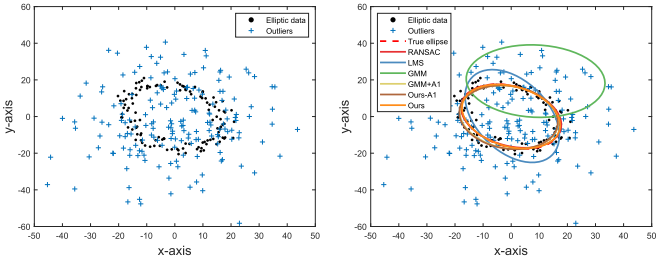

Fig. 8. Comparison of robust methods in terms of outliers. Left: Input data points containing 60% outliers. Right: Fitting results attained by different robust methods.

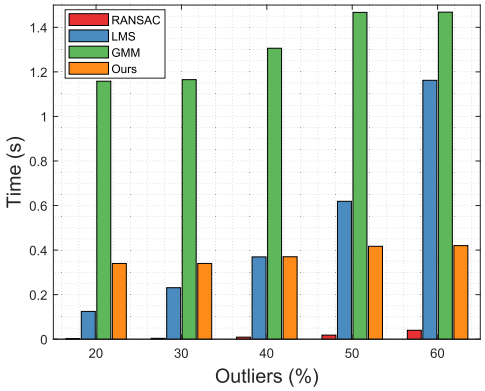

Fig. 9. Time comparison of robust methods under different outliers.

keeps sub-pixel errors under 60% outliers. However, both GMM and LMS report a 10^2 center deviation even at a small number of outliers. RANSAC also returns large deviations when the outliers exceed 40%. For angle deviation, our method embraces the smallest MSE and keeps utmost stable. Note that the MSE of RANSAC experiences a rapid growth when the outliers exceed 30%. For semi-axis deviation, the MSE scope of our method mainly lies in $[10^{-2}, 1]$, thereby highlighting its strong robustness against outliers. Apart from LMS and GMM that show large deviations for the semi-axis, RANSAC also shows weakness to substantial outliers. We present an example in Fig. 8.

We also report the average time consumption of the 200 implementations in Fig. 9. As observed, RANSAC has the lowest time consumption, whereas GMM has the largest time consumption. Given that the iterative interval of the bandwidth in each layer has been narrowed down in our method, our running time is significantly shorter than that of GMM, and remains highly stable under different outlier levels. By contrast, with the outliers increasing, the time consumption

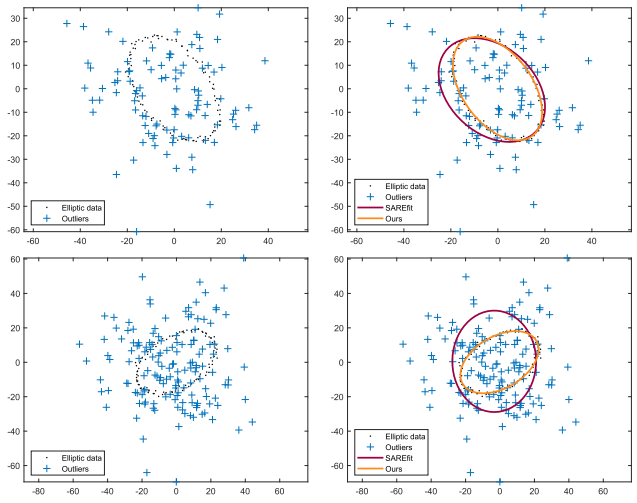

Fig. 10. Comparison examples of the proposed method with SAREfit [48]. As observed, the ellipse fitting results of SRAEfit show significant deviations, in contrast, our method attains successful fittings for both cases.

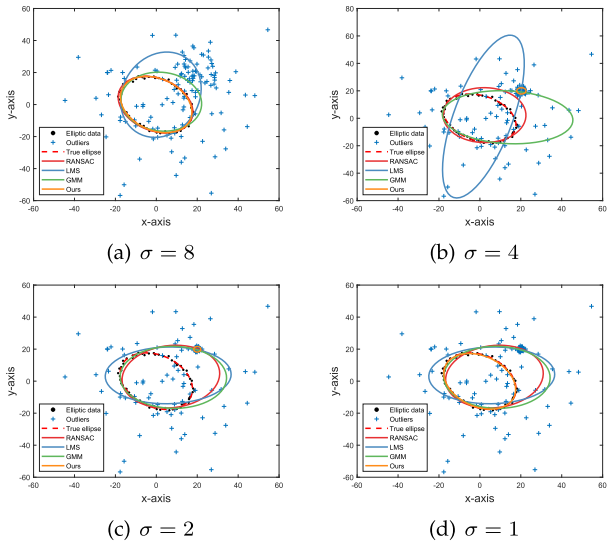

(a) $\sigma = 8$ (b) $\sigma = 4$ (c) $\sigma = 2$ (d) $\sigma = 1$

Fig. 11. Comparisons regarding to clustered outliers. As the standard variance (σ) of clustered outliers getting smaller, all methods are affected. However, our method can circumvent this problem through a straightforward detection of clustered outliers, and the ellipse fitting result is shown in the last image.

of LMS rapidly increases, thereby indicating its numerous iterations.

Furthermore, we compare our algorithm to a latest method called SAREfit [48] dedicated for outliers, in which uniform sampling and L_1 median techniques are adopted. To be fair, we use the same parameter setting as the previous outlier test. Its results are reported in Table IV. As observed, SAREfit produces less center deviations than GMM, but its deviations are still significant compared with RANSAC and ours. The rotation angle of SAREfit is fluctuated, indicating its instability. When the outlier percentage is less than 30%, the fitted semi-axis length is acceptable. However, with outliers increasing, SAREfit produces more noticeable axis deviations. Several examples are presented in Fig. 10.

4) Clustered Outliers: Our method exhibits a promising performance amid the presence of outliers from a uniform distribution. In this test, we further explore the influence of clustered outliers on ellipse fitting. As shown in Fig. 11, we generate an ellipse corrupted by outliers both in uniform and clustered configurations. The clustered outliers have four different standard variances ($\sigma = 8, 4, 2, 1$). A smaller σ corresponds to more gathered clustered outliers. Figs. 11(a) to (c) shows that all methods are affected by the clustered outliers, which attract the fitted ellipses to themselves. However, the ellipse E fitted by our method always envelops the high-density region by working on point density. To utilize this feature, we initially count the number of points M lying inside E, and then compute the area πab of E. If $M/(\pi ab) > 0.9$, then we consider this region formed by clustered outliers, and remove the points inside E together with its surrounding points. This intuitive strategy significantly improves the robustness of ellipse fitting against clustered outliers as illustrated in Fig. 11(d).

5) Ablation Study: Given that our method consists of two parts for ellipse fitting, we perform an ablation study to reveal the effect of each part.

a) Effect of the Center of the Growing Region R: We remove the first part of our algorithm (A1) and simply choose the barycenter of the input data points as the initial position. The fitting results denoted by HGMM(Ours)-A1 are reported in Table IV. HGMM(Ours)-A1 produces more center deviations than HGMM(Ours), and obvious fluctuations in the semi-axis estimation can be seen. The MSE of HGMM(Ours)-A1 is presented in Fig. 7, which shows that HGMM(Ours)-A1 returns more deviations for the geometric parameters, especially for centers and semi-axes. The significant gaps between HGMM(Ours)-A1 and HGMM(Ours) demonstrate the effectiveness of the proposed region growing strategy.

b) Effect of the Distance-Density Scheme: We use the same elliptic parameter attained by A1 as the initial value for GMM and HGMM(ours), and the statistic results of the improved GMM, which we call GMM + A1, are recorded in Table IV. The fitting accuracy of GMM shows obvious enhancement, especially for the center estimation. As shown in Fig. 7, compared with that to GMM, the overall MSE of GMM + A1 largely decreases. Nevertheless, due to the loss of correct ellipses as demonstrated in Section VI-A, GMM + A1 still shows significant deviations compared with our method. Therefore, the distance-density based scheme can guarantee more accurate ellipse fitting and outperforms its competitors.

6) Multiple Ellipse Fitting: Besides single-ellipse cases, multiple ellipses often exist in practice. When fitting one of these ellipses, the others become pseudo-outliers. To test the robustness of our proposed method against pseudo-outliers, similar to [49], we generate three configurations of four ellipses, namely, *disjoint*, *nested*, and *overlapped*, as illustrated in Fig. 12. Each ellipse contains 120 points and is disturbed by Gaussian noise with zero mean and $\sigma = 50\%$. Additionally, we generate 480 uniformly distributed outliers in the range $(-60, 60)$. Therefore, the percentage of outliers is 50%. Note that for the first fitting, except for the outliers, the other three ellipses are seen as pseudo-outliers ($120 \times 3 = 360$), thus we have a total of 840 outliers ($360 + 480 = 840$).

The fitting results are illustrated in the second row of Fig. 12. Given that the initial location of GMM is chosen randomly and the interference of substantial outliers, its fitting results are far from satisfactory. In addition, LMS

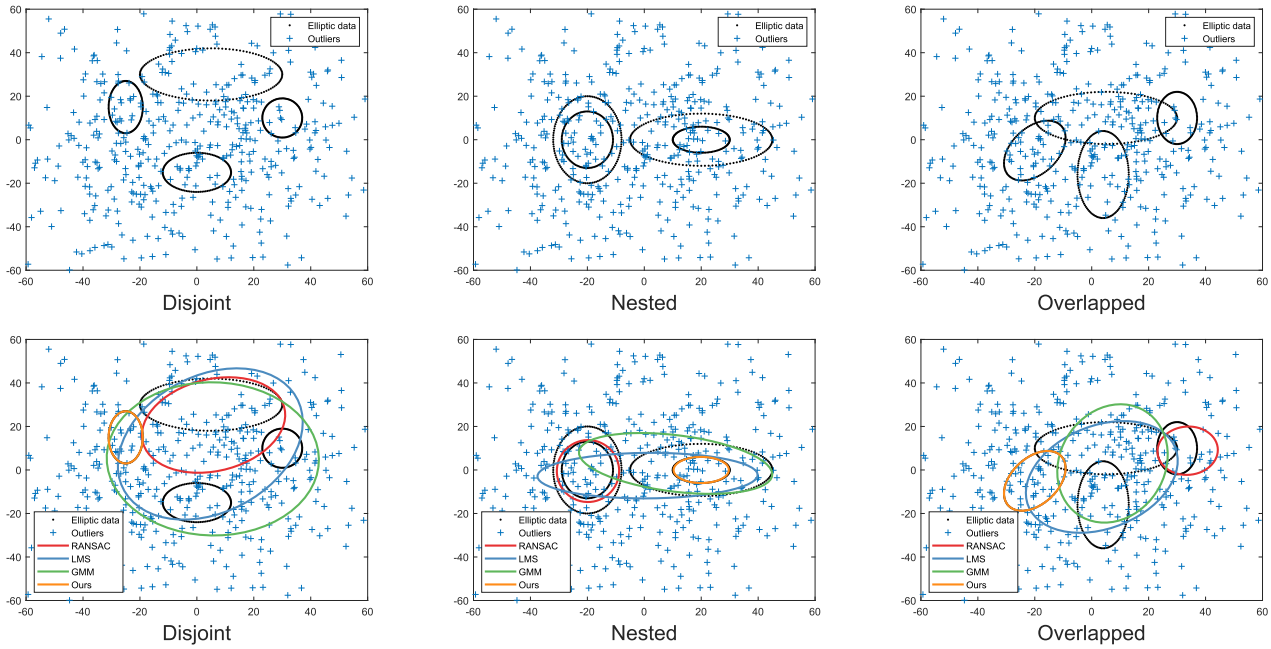

Fig. 12. Top: Three configurations, including disjoint, nested, and overlapped. Bottom: Fitting results attained by the four robust methods.

also reports unsatisfactory results. However, RANSAC obtains relatively better results than GMM and LMS in the nested and overlapped configurations, but RANSAC shows evident deviations for the three cases, especially for disjoint configuration. Meanwhile, our proposed method exhibits a stable performance and successfully fits one of the correct ellipses for all configurations.

Similar to RANSAC, our proposed method can be directly used for multiple ellipse fitting in a single run. For each fitted ellipse $\hat{\theta} = (x_0, y_0, a, b, \gamma)$, we compute its perimeter by using Ramanujan's approximate formula [50]: $P \approx \pi(3(a+b) - \sqrt{(3a+b)(a+3b)})$. Afterward, the point whose distance to $\hat{\theta}$ is no greater than two is seen as an inlier, and the total number of inliers is counted as n. A fitted ellipse is considered a true positive if $n/P \geq 0.7$, otherwise, this ellipse is unreliable and is removed from the candidate ellipses together with the corresponding data points. This process continues until no correct ellipses reported after two consecutive fittings. Different from RANSAC, which iteratively fits randomly sampled points, our method locates and fits high density points, which are more likely from ellipses. We test above technique for intersected ellipses in Fig. 4 (c) and previous three configurations. The results are presented in the first two rows of Fig. 13, in which we successfully fit all the two intersected ellipses, and shows potential capability for complex configurations. Furthermore, we enlarge the variance of the Gaussian noise for ellipse data in Fig. 4 (c), and contaminate the data by heavy outliers, as shown in the third row of Fig. 13, where ellipse data and outliers share similar density. We still implement the proposed method one time and the fourth row shows the results. As observed, our method attains satisfactory fittings for all cases although the outlier disturbance and density variation, accompanying videos can be found in the supplemental material.

7) Parameter Analysis: Our method mainly involves three parameters, *i.e.*, the bandwidth h, the number of points N in the growing region R, and the neighborhood scope ϵ of $\mathbf{x}_0$. We experimentally investigate the influences of these parameters on ellipse fitting.

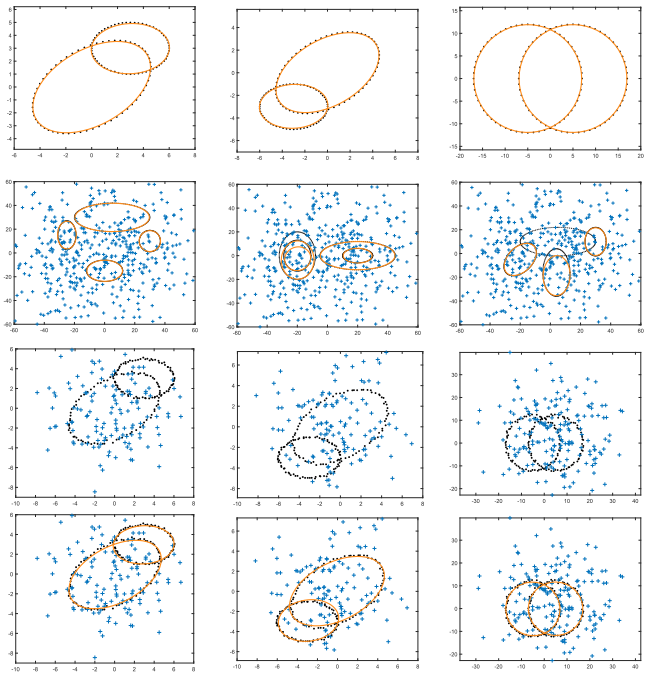

Fig. 13. Multiple ellipse fitting by running the proposed method one time. Our method successfully fits the two intersected ellipses, even under the disturbance of outliers and density variation, meanwhile showing its potential for the three complex configurations.

(1). The bandwidth h acts as a smoothing parameter in kernel density estimation. Choosing h, also called bandwidth selection, is a classical research topic in non-parametric

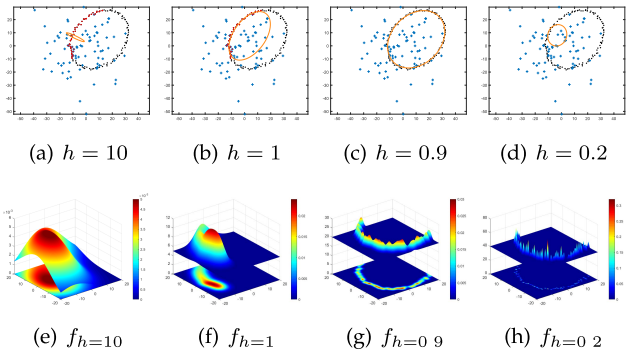

(a) $h = 10$ (b) $h = 1$ (c) $h = 0.9$ (d) $h = 0.2$

(e) $f_{h=10}$ (f) $f_{h=1}$ (g) $f_{h=0\ 9}$ (h) $f_{h=0\ 2}$

Fig. 14. Analysis of the influences of variation of h on the ellipse fitting. The top row presents the fitting results attained by the outer and inner layers based on different h, whereas the bottom row presents the images of the data model $f_h = f(\mathbf{x}|\theta, h)$ including its top view.

statistics [51]. Although the best h cannot be easily decided, we can attain insights into how to choose a proper h from the following experiments. As shown in Fig. 14, an ellipse contaminated by noise and outliers is randomly generated. Figs. 14 (a) and (b) present the outer fitting results obtained by setting $h \in [10, 5]$ and $h \in [4, 1]$, respectively. The result of the first h exhibits more deviations than the second one. To get more insights, we further visualize the data model $f(\mathbf{x}|\theta, h)$ along with its top view for the growing region by equating $h = 10$ and $h = 1$ in Figs. 14 (e) and (f), respectively. From which, we see that $f(\mathbf{x}|\theta, h = 10)$ is much smoother than $f(\mathbf{x}|\theta, h = 1)$, hence the former will produce an over-smoothing effect on some structures or wash them out in the data points. By contrast, $f(\mathbf{x}|\theta, h = 1)$ maintains the elliptic structure. Based on the outer fitting, the inner layer has the settings $h \in [0.9, 0.6]$ and $h \in [0.5, 0.2]$, and the results are presented in Figs. 14 (c) and (d). We also present the images of $f(\mathbf{x}|\theta, h = 0.9)$ and $f(\mathbf{x}|\theta, h = 0.2)$, where the latter is more noisy than the former. Therefore, $f(\mathbf{x}|\theta, h = 0.2)$ pays more attention to the local structure, leading to much smaller fitting results. We suggest using $h \in [4, 1]$ and $h \in [0.9, 0.6]$ for the outer and inner layers, respectively.

(2). To analyze the effect of N and ϵ on the growing region, we first fix $N = 50$ and $\epsilon = 10$, and the growing region is shown in Fig. 15(a). Afterward, we enlarge the ellipse several times, such as $\times 2$, $\times 3$, and $\times 4$, as illustrated in Figs. 15(b) to (d). When the time is less than $\times 4$, the growing region remains satisfactory. However, when the ellipse is quite large, the distance among the neighborhood points also increases, thereby leaving few points in the growing region. To address this problem, we set $\epsilon = 40$. The growing region and fitted ellipse are presented in Figs. 15(e) to (f), which again attains an accurate fitting. Therefore, for quite large ellipses, to achieve better performance, we suggest slightly increase ϵ.

(3). We further test the influences of N on ellipse fitting. To this end, we contaminate the ellipse by a series of outliers in percentage of $P \in \{30\%, 35\%, 40\%, 50\%\}$ as shown in Figs. 15(g) to (j). We find that the parameter setting $N = 50$ and $\epsilon = 10$ can help our method successfully fit ellipses with outliers of less than 50%. When $P \geq 50\%$, the outliers start to be considered as inliers, thereby biasing the fitted ellipse. To embrace more inliers, we enlarge $N = 70$. Afterward, the fitted ellipse becomes satisfactory as shown in Fig. 15(k). We further contaminate the ellipse by 70% outliers and set $N = 80$. Our method continues to achieve accurate fitting. Accordingly, when the input data points are corrupted by a quite large amount of outliers, we can increase N to improve the fitting accuracy.

D. Real Images

We have implemented a series of experiments on 2D point clouds. Apart from performing synthetic tests where an evaluation is possible, we also assess the performance of our proposed method for real images.

1) Occluded Images: We first apply the proposed method to fit ellipses with occlusion. We use the dataset provided in [52], which contains six sub-datasets, and each sub-dataset has 50 images with $\beta \in \{4, 8, 12, 16, 20, 24\}$ occluded ellipses. To fit the ellipses, we first adopt the algorithm in [53] to attain elliptic arcs. This algorithm works by initially extracting the edge curves through the Canny detector [54] and subsequently approximating them by using a set of line segments followed by the split at sharp corners and inflection points. For instance, given an image with four occluded ellipses, the extracted elliptic arcs are presented in Fig. 16(a), where different colors indicate different arcs. As can be seen, an elliptic edge may be split into several arcs. Actually, the coexistence of short and long fragments and ellipses with high and low eccentricity is often encountered in practice. To relieve the ellipse fitting biases caused by short arcs, previous ellipse detectors [55]–[57] usually need to group together those arcs from the same ellipse. However, this procedure is not necessary for our method. Specifically, we initially sort the arcs based on their length and then start the ellipse fitting from the longest segment. This procedure is actually the outer fitting process used in HGMM. Afterward, the inner fitting is invoked facing all arcs to further enhance the fitting accuracy. The pipeline is illustrated in Fig. 16. After each fitting, we remove the edge points whose distance from the fitted ellipse is no greater than 2. This process continues until no elliptic arcs are left.

To objectively compare our method with others, we adopt three well-known metrics from information retrieval to our context, namely, *precision*, *recall*, and *F-measure*, which are defined as precision $= |\text{TP}|/|\text{TP} + \text{FP}|$, recall $= |\text{TP}|/|\text{TP} + \text{FN}|$, and F-measure $= 2/(\text{precision}^{-1} + \text{recall}^{-1})$.

A fitted ellipse E_f is seen as a true positive (TP) if its overlapping ratio regarding the ground truth E_t is no less than 0.9, otherwise this ellipse is a false positive (FP). Meanwhile, an incorrectly fitted ground truth is seen as a false negative (FN). We follow the manner in [52] to define the overlapping ratio between E_f and E_t:

$$\text{OverlapRatio}(E_f, E_t) = \frac{area(E_f) \cap area(E_t)}{area(E_f) \cup area(E_t)},$$

where $area(E_*)$ denotes the number of pixels inside the ellipse E_*. The fitting results are presented in Fig. 17. Our method reports the highest precision and F-measure under different occlusions and achieves the overall highest recall. By contrast, LS-based methods demonstrate poorer performance than ours, and GMM is much lower than them, thereby highlighting the benefit of the proposed hierarchical structure. Specifically, the outer layer only fits the designated elliptic arc and provides reasonable initial parameters, and then the inner layer, based on the outer parameter, is applied to the whole arcs to further improve fitting accuracy. However, due

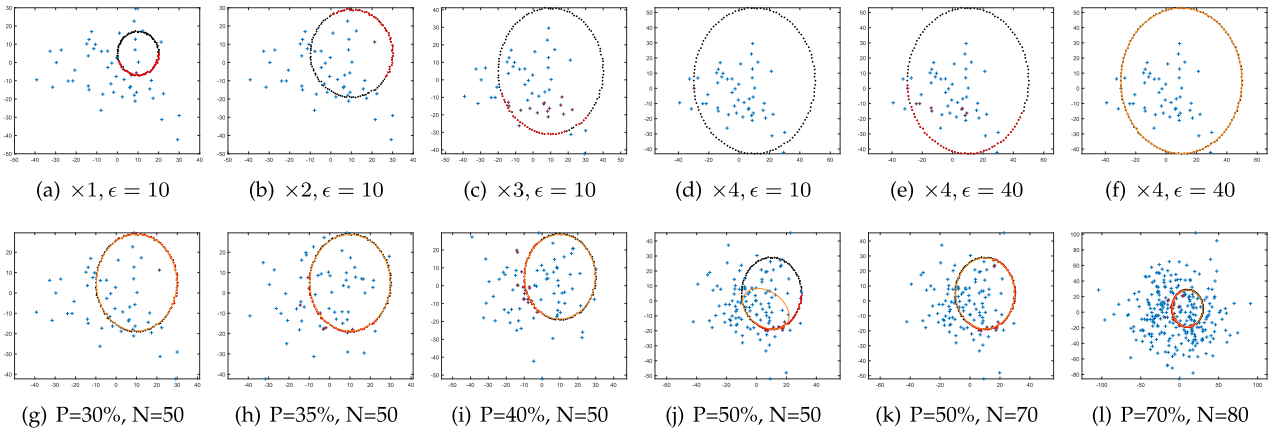

(a) $\times 1, \epsilon = 10$ (b) $\times 2, \epsilon = 10$ (c) $\times 3, \epsilon = 10$ (d) $\times 4, \epsilon = 10$ (e) $\times 4, \epsilon = 40$ (f) $\times 4, \epsilon = 40$

(g) P=30%, N=50 (h) P=35%, N=50 (i) P=40%, N=50 (j) P=50%, N=50 (k) P=50%, N=70 (l) P=70%, N=80

Fig. 15. Investigation of the effect of neighborhood distance ϵ of $\mathbf{x}_0$ (top) and the number of points N in the growing region (bottom) on the ellipse fitting. To get better performance, when the ellipse is quite large, we can slightly increase ϵ. Similarly, when heavy outliers are present, we can also choose a larger N.

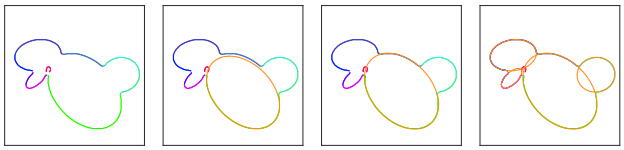

(a) Input arcs (b) Outer fitting (c) Inner fitting (d) Final fitting

Fig. 16. The pipeline of ellipse fitting for occluded cases. The outer layer fits the longest segmented arc individually, and then the inner layer considers all arcs to further improve the fitting accuracy.

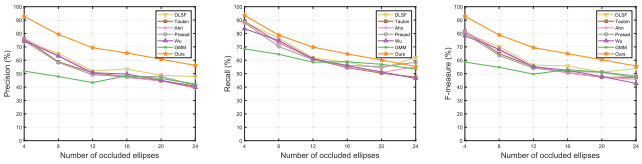

Fig. 17. Statistic results of occluded ellipses. From left to right: Results of precision, recall, and F-measure. Thanks to the hierarchical structure, our method achieves the best performance among all compared methods.

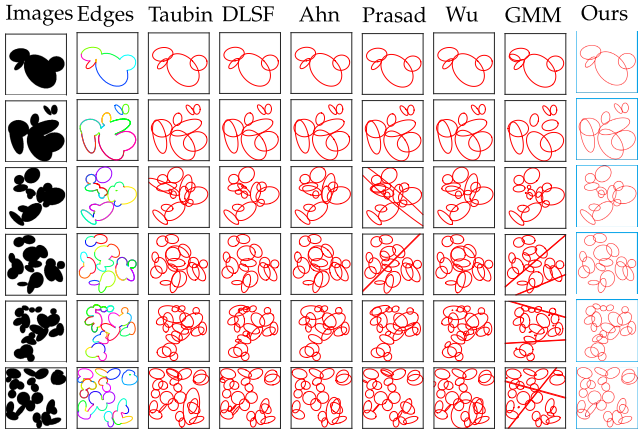

Fig. 18. Fitting comparison of β occluded ellipses ($\beta \in \{4, 8, 12, 16, 20, 24\}$). The fine results are highlighted by the blue boxes. Our method almost successfully fits all ellipses.

to the splitting of ellipses, LS-based methods may observe major fitting deviations for small elliptic arcs, especially for arcs with a small curvature. A comparison result is presented in Fig. 18. Additional comparison images are provided in the supplemental material, together with a fitting demo.

2) Iris Recognition: We then examine ellipse fitting for iris images. As a biometric identification technique, iris recognition plays an important role in real-life applications. A key step in iris recognition is identifying the pupil region of the human eye and localizing the iris [41]. However, outliers are often observed in practice, such as the interference of spectral reflections. See the image in Fig. 19(a) for reference.

We apply the proposed method to fit the boundaries of the iris and pupil for the images in Figs. 19(a) and (e). To this end, Canny detector is first used to extract the edge curves. The threshold values used in the detector are set to $[0.03, 0.09]$. Afterward, we perform image segmentation to obtain the edge contours. The extracted boundaries are presented in Figs. 19(b) and (f), where the red pixels indicate the inner boundaries and the black pixels indicate the outer ones. Several outliers can be observed in the inner boundaries, which affect the accuracy of ellipse fitting. Additionally, given the interference of the eye lid and eye lashes, the upper bounds of the iris are partially occluded, thereby disturbing the fitting performance. To simplify the fitting process, we directly take the whole points as the outer layer input. The fitting results of our method are presented in Figs. 19(c) and (g). As observed, the fitted ellipses match the boundaries well, thereby achieving a reliable localization for irises and pupils. We also compare the proposed method with others and report the results in Figs. 19(d) and (h). Fig. 19(d) shows that the other methods produce smaller ellipses than ours for the outer boundary fitting. Moreover, as the outliers increase, the other methods tend to produce large deviations as shown in Fig. 19(h). Notably, Ahn and Prasad return no results in this case.

3) Spacecraft Location: Pose estimation of spacecrafts is a common astronautic task, and their outlines are projected as ellipses. In this experiment, we apply the proposed method to fit the ellipses for a spacecraft image, which is helpful for the subsequent pose determination. The Voyager 1 image[2]

[2]https://mobilemag.com/2013/03/22/voyager-1-where-is-it/

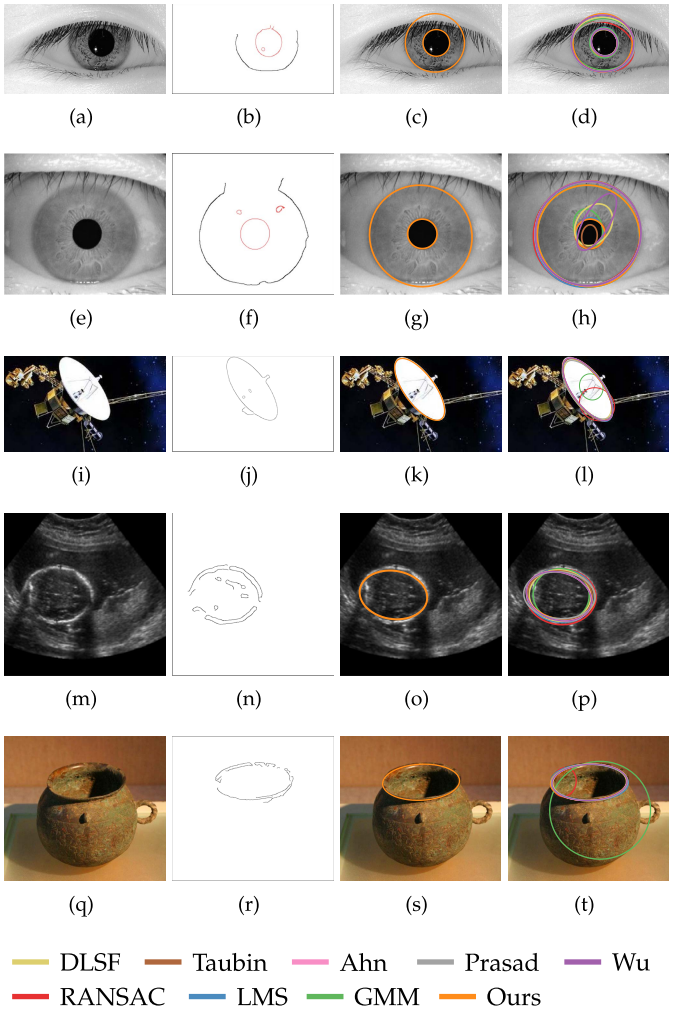

Fig. 19. Ellipse fitting for iris recognition (first two rows), spacecraft location (third row), fetal abdomen segmentation (fourth row), and antique caliber measurement (last row). Left to right columns: Input images, extracted edge segments, fitting results attained by our method, and fitting results attained by all compared methods.

shown in Fig. 19(i) is used in this experiment. The edge contours extracted from this image is presented in Fig. 19(j). These contours are obtained after the Canny edge detection (the threshold is [0.03, 0.09]) and image segmentation. Several outliers are observed due to the spacecraft structure. The ellipses obtained by the proposed method and those obtained by all compared methods are shown in Figs. 19(k) and (l), respectively. As can be seen, the LS-based methods achieve a fine fitting yet report some deviations. By contrast, the proposed method achieves preferable results due to its robustness. Meanwhile, RANSAC and GMM produce large deviations that indicate their instability.

4) Ultrasound Fetal Segmentation: In this experiment, we apply the proposed method for fetal abdomen segmentation in ultrasound images. Duly monitoring fetal growth is very important for prenatal care. Fetal abdomen circumference (AC) is relevant to fetal growth and is an effective index for fetal weight estimation [58]. In practice, fetal abdomen segmentation is a useful procedure for AC measurement. We deploy the proposed method to fit the ellipse that characterizes the fetal contour. An ultrasound fetal image is presented

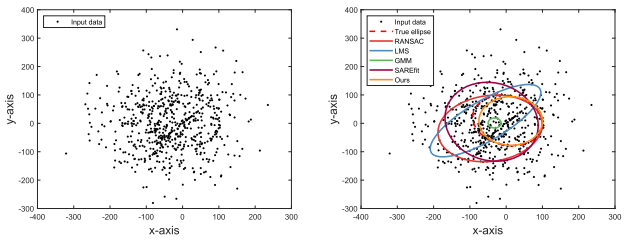

Fig. 20. When the ellipse data and outliers have the same density, the elliptic structure is no longer salient, thereby all robust methods return biased fittings.

in Fig. 19(m). The edge segments extracted via Canny edge detection ([0.03, 0.09]) and image segmentation are shown in Fig. 19(n). Given the nature of the image, there inevitably exist outliers. The fitting results of the proposed method and the other methods are reported in Figs. 19(o) and (p), respectively. Our proposed method provides a relatively satisfactory estimation, whereas Ahn and Wu largely deviate from the ground truth as seen from their rotation angles. Meanwhile, GMM produces an evidently smaller estimation, whereas Prasad produces the largest estimation among all methods.

5) Antique Measurement: We also apply the proposed method to an interesting measurement for the antique caliber. To avoid manual contaminations, we estimate the elliptic parameter from the antique image and then restore the true value with known camera intrinsics. The bottom of Fig. 19 shows a pottery antique[3] with extracted edge segments. The fitting results of our method and the other compared methods are reported in Figs. 19(s) and (t). Although the edge has been disturbed as several segmented fragments, the ellipse fitting result of our method is still quite close to the ground truth. The LS-based methods report similar results. However, both RANSAC and GMM produce significant deviations.

VII. Discussion and Conclusion

We have presented a robust and accurate method for ellipse fitting in noisy, outliers-contained, and occluded environments. Our first contribution lies in the investigation of cases where GMM fails to fit the correct ellipses. We propose a novel metric that combines distance and density for ellipse fitting and is reliable for determining correct ellipses. We also propose a framework that expands GMM to two hierarchical layers, of which the outer layer is designed to provide reasonable initial parameters that are estimated from a density-based region growing scheme and the inner layer is applied to the whole data to further improve fitting accuracy. The performance of the new method is compared with that of eight representative state-of-the-art methods by performing versatile experiments on synthetic images and real images. Owing to the hierarchical structure, our method shows significant improvements in its robustness against outliers, demonstrates promising performance, and narrows down the iterative interval of the bandwidth, thereby accelerating the fitting process. Our code is available at https://github.com/zikai1/HGMMEllFit.

Since our method involves the density comparison, it is difficult to recover the true ellipses when ellipse points and outliers have the same density as shown in Fig. 20. However, all robust methods fail to deal with such cases. The reason

[3]http://www.linzi.gov.cn/art/2016/2/18/art_6443_1092234.html

is that the elliptic structure is no longer salient among the input data, and algorithms take all points as the target ellipse. Nevertheless, as demonstrated in previous experiments, our method works well for most scenarios. To circumvent this remarkably difficult problem, a probably feasible way is to explore more geometric properties of ellipses and cast it into an ellipse detection framework.

Although the proposed method is aimed toward ellipse fitting, by rebuilding the model $g(\mathbf{x}|\boldsymbol{\theta})$ on the basis of the different conics characterized by $\boldsymbol{\theta}$, the proposed framework can easily be generalized to fit other conics under noise/outlier settings. An interesting direction for future research is to generalize the method to fit 3D geometric primitives, such as spheres, ellipsoids, and cylinders in point clouds. For this case, apart from the distribution of data points, one can explore more useful geometric features, such as normals and curvatures, and encapsulate them into the data model $f(\boldsymbol{x})$ by an anisotropic covariance matrix to achieve a more accurate fitting. Additionally, exploiting efficient optimization methods for the 3D geometric parameters, for instance, nine parameters for ellipsoids, or by means of deep learning techniques, present other directions for the future work.

REFERENCES

[1] F. K. Chan *et al.*, *Spacecraft Collision Probability*. El Segundo, CA, USA: Aerospace Press, 2008.

[2] Y. Liu *et al.*, "A practical detection of non-cooperative satellite based on ellipse fitting," in *Proc. IEEE Int. Conf. Mechatronics Autom.*, Aug. 2016, pp. 1541–1546.

[3] Q. Chen, H. Wu, S. Higashino, and R. Sakamoto, "Camera calibration by recovering projected centers of circle pairs," in *Proc. ACM SIGGRAPH Posters*, Jul. 2016, p. 39.

[4] H. Huang, H. Zhang, and Y.-M. Cheung, "The common self-polar triangle of concentric circles and its application to camera calibration," in *Proc. IEEE Conf. Comput. Vis. Pattern Recognit. (CVPR)*, Jun. 2015, pp. 4065–4072.

[5] H.-S. Kim, W.-S. Kang, J.-I. Shin, and S.-H. Park, "Face detection using template matching and ellipse fitting," *IEICE Trans. Inf. Syst.*, vol. 83, no. 11, pp. 2008–2011, 2000.

[6] R.-L. Hsu, M. Abdel-Mottaleb, and A. K. Jain, "Face detection in color images," *IEEE Trans. Pattern Anal. Mach. Intell.*, vol. 24, no. 5, pp. 696–706, May 2002.

[7] M. Kassner, W. Patera, and A. Bulling, "Pupil: An open source platform for pervasive eye tracking and mobile gaze-based interaction," in *Proc. ACM Int. Joint Conf. Pervas. Ubiquitous Comput., Adjunct Publication*, Sep. 2014, pp. 1151–1160.

[8] A. Talukder, J.-M. Morookian, S. Monacos, R. Lam, C. LeBaw, and J. L. Lambert, "Eye-tracking architecture for biometrics and remote monitoring," *Appl. Opt.*, vol. 44, no. 5, pp. 693–700, 2005.

[9] N. Kharma *et al.*, "Automatic segmentation of cells from microscopic imagery using ellipse detection," *IET Image Process.*, vol. 1, no. 1, pp. 39–47, Mar. 2007.

[10] X. Bai, C. Sun, and F. Zhou, "Splitting touching cells based on concave points and ellipse fitting," *Pattern Recognit.*, vol. 42, no. 11, pp. 2434–2446, Nov. 2009.

[11] S. Kothari, Q. Chaudry, and M. D. Wang, "Automated cell counting and cluster segmentation using concavity detection and ellipse fitting techniques," in *Proc. IEEE Int. Symp. Biomed. Imag., Nano Macro*, Jun. 2009, pp. 795–798.

[12] J. Li *et al.*, "Automatic fetal head circumference measurement in ultrasound using random forest and fast ellipse fitting," *IEEE J. Biomed. Health Informat.*, vol. 22, no. 1, pp. 215–223, Jan. 2018.

[13] S. P. Rajan and V. Kavitha, "Diagnosis of cardiovascular diseases using retinal images through vessel segmentation graph," *Current Med. Imag. Rev.*, vol. 13, no. 4, pp. 454–459, Nov. 2017.

[14] P. V. Hough, "Method and means for recognizing complex patterns," U.S. Patent 3 069 654, Dec. 18, 1962.

[15] R. C. Bolles and M. A. Fischler, "A RANSAC-based approach to model fitting and its application to finding cylinders in range data," in *Proc. IJCAI*, 1981, pp. 637–643.

[16] B. Jian and B. C. Vemuri, "Robust point set registration using Gaussian mixture models," *IEEE Trans. Pattern Anal. Mach. Intell.*, vol. 33, no. 8, pp. 1633–1645, Aug. 2011.

[17] C. Arellano and R. Dahyot, "Robust ellipse detection with Gaussian mixture models," *Pattern Recognit.*, vol. 58, pp. 12–26, Oct. 2016.

[18] K. Kanatani, Y. Sugaya, and Y. Kanazawa, "Ellipse fitting for computer vision: Implementation and applications," *Synth. Lectures Comput. Vis.*, vol. 6, no. 1, pp. 1–141, Apr. 2016.

[19] A. Fitzgibbon, M. Pilu, and R. B. Fisher, "Direct least square fitting of ellipses," *IEEE Trans. Pattern Anal. Mach. Intell.*, vol. 21, no. 5, pp. 476–480, May 1999.

[20] S. J. Ahn, W. Rauh, and H.-J. Warnecke, "Least-squares orthogonal distances fitting of circle, sphere, ellipse, hyperbola, and parabola," *Pattern Recognit.*, vol. 34, no. 12, pp. 2283–2303, Dec. 2001.

[21] P. L. Rosin and G. A. W. West, "Nonparametric segmentation of curves into various representations," *IEEE Trans. Pattern Anal. Mach. Intell.*, vol. 17, no. 12, pp. 1140–1153, 1995.

[22] Z. L. Szpak, W. Chojnacki, and A. Van Den Hengel, "Guaranteed ellipse fitting with the Sampson distance," in *Proc. Eur. Conf. Comput. Vis.* Cham, Switzerland: Springer, 2012, pp. 87–100.

[23] G. Taubin, "Estimation of planar curves, surfaces, and nonplanar space curves defined by implicit equations with applications to edge and range image segmentation," *IEEE Trans. Pattern Anal. Mach. Intell.*, vol. 13, no. 11, pp. 1115–1138, Nov. 1991.

[24] D. K. Prasad, M. K. H. Leung, and C. Quek, "ElliFit: An unconstrained, non-iterative, least squares based geometric ellipse fitting method," *Pattern Recognit.*, vol. 46, no. 5, pp. 1449–1465, May 2013.

[25] Y. Wu, H. Wang, F. Tang, and Z. Wang, "Efficient conic fitting with an analytical polar-N-direction geometric distance," *Pattern Recognit.*, vol. 90, pp. 415–423, Jun. 2019.

[26] P. J. Rousseeuw and A. M. Leroy, *Robust Regression and Outlier Detection*, vol. 589. Hoboken, NJ, USA: Wiley, 2005.

[27] P. J. Rousseeuw, "Least median of squares regression," *J. Amer. Statist. Assoc.*, vol. 79, no. 388, pp. 871–880, 1984.

[28] V. F. Leavers, *Shape Detection in Computer Vision Using the Hough Transform*. Cham, Switzerland: Springer, 1992.

[29] F. Duan, L. Wang, and P. Guo, "RANSAC based ellipse detection with application to catadioptric camera calibration," in *Proc. Int. Conf. Neural Inf. Process.* Cham, Switzerland: Springer, 2010, pp. 525–532.

[30] H. Wang and D. Suter, "MDPE: A very robust estimator for model fitting and range image segmentation," *Int. J. Comput. Vis.*, vol. 59, no. 2, pp. 139–166, Sep. 2004.

[31] N. Kiryati, Y. Eldar, and A. M. Bruckstein, "A probabilistic Hough transform," *Pattern Recognit.*, vol. 24, no. 4, pp. 303–316, Jan. 1991.

[32] H. Li, M. A. Lavin, and R. J. Le Master, "Fast Hough transform: A hierarchical approach," *Comput. Vis., Graph., Image Process.*, vol. 36, nos. 2–3, pp. 139–161, Nov. 1986.

[33] L. Xu, E. Oja, and P. Kultanen, "A new curve detection method: Randomized Hough transform (RHT)," *Pattern Recognit. Lett.*, vol. 11, no. 5, pp. 331–338, May 1990.

[34] W. Lu, J. Tan, and R. Floyd, "Automated fetal head detection and measurement in ultrasound images by iterative randomized Hough transform," *Ultrasound Med. Biol.*, vol. 31, no. 7, pp. 929–936, Jul. 2005.

[35] P. H. S. Torr and A. Zisserman, "MLESAC: A new robust estimator with application to estimating image geometry," *Comput. Vis. Image Understand.*, vol. 78, no. 1, pp. 138–156, Apr. 2000.

[36] B. J. Tordoff and D. W. Murray, "Guided-MLESAC: Faster image transform estimation by using matching priors," *IEEE Trans. Pattern Anal. Mach. Intell.*, vol. 27, no. 10, pp. 1523–1535, Oct. 2005.

[37] V. Rodehorst and O. Hellwich, "Genetic algorithm SAmple consensus (GASAC)—A parallel strategy for robust parameter estimation," in *Proc. Conf. Comput. Vis. Pattern Recognit. Workshop (CVPRW)*, Jun. 2006, p. 103.

[38] D. S. Barwick, "Very fast best-fit circular and elliptical boundaries by chord data," *IEEE Trans. Pattern Anal. Mach. Intell.*, vol. 31, no. 6, pp. 1147–1152, Jun. 2009.

[39] P. K. J. Cai and S. Miklavcic, "Improved ellipse fitting by considering the eccentricity of data point sets," in *Proc. IEEE Int. Conf. Image Process.*, Sep. 2013, pp. 815–819.

[40] B. Matei and P. Meer, "Reduction of bias in maximum likelihood ellipse fitting," in *Proc. 15th Int. Conf. Pattern Recognit. (ICPR)*, vol. 3, 2000, pp. 794–798.

[41] J. Liang, Y. Wang, and X. Zeng, "Robust ellipse fitting via half-quadratic and semidefinite relaxation optimization," *IEEE Trans. Image Process.*, vol. 24, no. 11, pp. 4276–4286, Nov. 2015.

[42] S. Mulleti and C. S. Seelamantula, "Ellipse fitting using the finite rate of innovation sampling principle," *IEEE Trans. Image Process.*, vol. 25, no. 3, pp. 1451–1464, Mar. 2016.
[43] J. Liang *et al.*, "Robust ellipse fitting based on sparse combination of data points," *IEEE Trans. Image Process.*, vol. 22, no. 6, pp. 2207–2218, Jun. 2013.
[44] G. Roth and M. D. Levine, "Geometric primitive extraction using a genetic algorithm," *IEEE Trans. Pattern Anal. Mach. Intell.*, vol. 16, no. 9, pp. 901–905, 1994.
[45] A. Ray and D. C. Srivastava, "Non-linear least squares ellipse fitting using the genetic algorithm with applications to strain analysis," *J. Struct. Geol.*, vol. 30, no. 12, pp. 1593–1602, Dec. 2008.
[46] W. Dong, P. Roy, C. Peng, and V. Isler, "Ellipse R-CNN: Learning to infer elliptical object from clustering and occlusion," *IEEE Trans. Image Process.*, vol. 30, pp. 2193–2206, Jan. 2021.
[47] F. Jeune, R. Deriche, R. Keriven, and P. Fua, "Tracking of hand's posture and gesture," CERTIS, ENPC, Res. Rep. 04-02, 2004.
[48] K. Thurnhofer-Hemsi, E. López-Rubio, E. B. Blázquez-Parra, M. C. Ladrón-de-Guevara-Muñoz, and Ó. D. de-Cózar-Macias, "Ellipse fitting by spatial averaging of random ensembles," *Pattern Recognit.*, vol. 106, Oct. 2020, Art. no. 107406.
[49] H. C. Hernández and L. G. de la Fraga, "A multi-objective robust ellipse fitting algorithm," in *Proc. NEO*. Cham, Switzerland: Springer, 2018, pp. 141–158.
[50] S. Ramanujan, "Modular equations and approximations to π," *Quart. J. Math.*, vol. 45, pp. 350–372, 1914.
[51] C. M. Bishop, *Pattern Recognition and Machine Learning*. Cham, Switzerland: Springer, 2006.
[52] A. Y.-S. Chia, S. Rahardja, D. Rajan, and M. K. Leung, "A split and merge based ellipse detector with self-correcting capability," *IEEE Trans. Image Process.*, vol. 20, no. 7, pp. 1991–2006, Jul. 2011.
[53] D. K. Prasad, M. K. H. Leung, C. Quek, and S.-Y. Cho, "A novel framework for making dominant point detection methods non-parametric," *Image Vis. Comput.*, vol. 30, no. 11, pp. 843–859, Nov. 2012.
[54] J. Canny, "A computational approach to edge detection," *IEEE Trans. Pattern Anal. Mach. Intell.*, vols. PAMI–8, no. 6, pp. 679–698, Nov. 1986.
[55] C. Lu, S. Xia, M. Shao, and Y. Fu, "Arc-support line segments revisited: An efficient high-quality ellipse detection," *IEEE Trans. Image Process.*, vol. 29, pp. 768–781, 2020.
[56] Q. Jia, X. Fan, Z. Luo, L. Song, and T. Qiu, "A fast ellipse detector using projective invariant pruning," *IEEE Trans. Image Process.*, vol. 26, no. 8, pp. 3665–3679, Aug. 2017.
[57] V. Patraucean, P. Gurdjos, and R. Grompone Von Gioi, "Joint a contrario ellipse and line detection," *IEEE Trans. Pattern Anal. Mach. Intell.*, vol. 39, no. 4, pp. 788–802, Apr. 2017.
[58] S. Campbell and D. Wilkin, "Ultrasonic measurement of fetal abdomen circumference in the estimation of fetal weight," *BJOG, Int. J. Obstetrics Gynaecology*, vol. 82, no. 9, pp. 689–697, Sep. 1975.

Mingyang Zhao is currently pursuing the Ph.D. degree with the Key Laboratory of Mathematics Mechanization, Academy of Mathematics and Systems Science, Chinese Academy of Sciences (CAS). His research interests include object detection, especially on geometric primitives, and point set registration in computer vision and pattern recognition, as well as semi-definite optimization in machine learning.

Xiaohong Jia received the bachelor's and Ph.D. degrees from the University of Science and Technology of China in 2004 and 2009, respectively. She is currently an Associate Professor with the Key Laboratory of Mathematics Mechanization, Academy of Mathematics and Systems Science, Chinese Academy of Sciences (CAS). Her research interests include computer graphics, computer aided geometric design, and computational algebraic geometry.

Lubin Fan received the B.Sc. degree from Wuhan University in 2009 and the Ph.D. degree in mathematics from Zhejiang University in 2014. From 2014 to 2017, he was a Postdoctoral Fellow with the Visual Computing Center, King Abdullah University of Science and Technology (KAUST). He joined the Alibaba Group in 2017. He is currently a Senior Algorithm Engineer with the Alibaba DAMO Academy. His research interests include image and video processing, geometric processing, and procedural modeling.

Yuan Liang received the B.Sc. and Ph.D. degrees from Tsinghua University, China, in 2014 and 2019, respectively. He is currently an Algorithm Engineer with the Alibaba DAMO Academy. His research interests include interactive multimedia analysis and geometric processing from visual media.

Dong-Ming Yan received the bachelor's and master's degrees from Tsinghua University in 2002 and 2005, respectively, and the Ph.D. degree from The University of Hong Kong in 2010. He is currently a Professor with the National Laboratory of Pattern Recognition, Institute of Automation, Chinese Academy of Sciences (CAS). His research interests include computer graphics, computer vision, geometric processing, and pattern recognition.